Adv. Funct. Mater. ***2017***, 1701818

DOI: 10.1002/adfm.201701818

Copper(I) Thiocyanate (CuSCN) Hole-Transport Layers Processed from Aqueous Precursor Solutions and Their Application in Thin-Film Transistors and Highly Efficient Organic and Organometal Halide Perovskite Solar Cells

*Nilushi Wijeyasinghe, Anna Regoutz, Flurin Eisner, Tian Du, Leonidas Tsetseris, Yen-Hung Lin, Hendrik Faber, Pichaya Pattanasattayavong, Jinhua Li, Feng Yan, Martyn A. McLachlan, David J. Payne, Martin Heeney and Thomas D. Anthopoulos**

N. Wijeyasinghe, F. Eisner, Dr. Y.-H. Lin, Dr. H. Faber, Prof. T. D. Anthopoulos
Department of Physics and The Centre for Plastic Electronics
Imperial College London
London SW7 2AZ, UK

Dr. A. Regoutz, T. Du, Dr. D. J. Payne, Dr. M. A. McLachlan
Department of Materials and The Centre for Plastic Electronics
Imperial College London
Royal School of Mines, London SW7 2AZ, UK

Prof. L. Tsetseris
Department of Physics
National Technical University of Athens
Athens GR-15780, Greece

Dr. P. Pattanasattayavong
Department of Materials Science and Engineering
School of Molecular Science and Engineering
Vidyasirimedhi Institute of Science and Technology (VISTEC)
Rayong 21210, Thailand

Dr. J. Li, Prof. F. Yan
Department of Applied Physics
The Hong Kong Polytechnic University
Hung Hom, Kowloon, Hong Kong

Prof. M. Heeney
Department of Chemistry and The Centre for Plastic Electronics
Imperial College London, London SW7 2AZ, UK

Prof. T. D. Anthopoulos
Materials Science and Engineering, Division of Physical Sciences and Engineering
King Abdullah University of Science and Technology
Thuwal 23955-6900, Saudi Arabia
E-mail: thomas.anthopoulos@kaust.edu.sa

Keywords: Copper(I) thiocyanate; hole transport layers; organic solar cells; perovskite solar cells; transparent semiconductors and transistors

Abstract

We report the development of copper(I) thiocyanate (CuSCN) hole-transport layers (HTLs) processed from aqueous ammonia as a novel alternative to conventional n-alkyl sulfide solvents. Wide-bandgap (3.4–3.9eV) and ultrathin (3–5nm) layers of CuSCN are formed when the aqueous CuSCN-ammine complex solution is spin-cast in air and annealed at 100 ˚C. X-ray photoelectron spectroscopy confirms the high compositional purity of the formed CuSCN layers, while the high-resolution valence band spectra agree with first-principles calculations. Study of the hole transport properties using field-effect transistor measurements reveal that the aqueous-processed CuSCN layers exhibit a fivefold higher hole mobility than films processed from diethyl sulphide solutions with the maximum values approaching 0.1 $cm^2V^{-1}s^{-1}$. A further interesting characteristic is the low surface roughness of the resulting CuSCN layers, which in the case of solar cells helps to planarize the indium-tin-oxide anode. Organic bulk-heterojunction and planar organometal halide perovskite solar cells based on aqueous-processed CuSCN HTLs yield power conversion efficiency of 10.7% and 17.5%, respectively. Importantly, CuSCN-based cells consistently outperform devices based on poly(3,4-ethylenedioxythiophene) polystyrene sulfonate HTLs. This is the first report on CuSCN and devices processed via an aqueous-based synthetic route that is compatible with high-throughput manufacturing and paves the way for further developments.

1. Introduction

Copper(I) thiocyanate (CuSCN) is an inorganic, wide-bandgap (>3.4 eV),[1,2] molecular semiconductor that combines excellent hole-transport (*p*-type) characteristics with high optical transparency and attractive mechanical properties.[2–4] The use of CuSCN as the hole-transport layer (HTL) has been demonstrated in numerous emerging opto/electronic applications,[5] including thin-film transistors (TFTs) and integrated circuits,[2,4,6] organic photovoltaic (OPV)

cells,[7,8] hybrid perovskite solar cells,[9–11] and organic light emitting diodes (OLEDs).[12,13] CuSCN can be deposited at low-temperature using a range of solution-processing methods, which include spin-casting,[2,6,7] ink-jet printing,[14,15] doctor blading,[16] spray coating,[17,18] and electrochemical deposition.[19–21] The processing versatility of CuSCN on the other hand enables its combination with inexpensive, and often temperature sensitive, substrate materials such as plastic.[22] These attractive physical attributes combined with its low cost and commercial availability make CuSCN a promising alternative to traditional inorganic/organic HTL materials.

Alternative materials that combine the processing versatility of CuSCN with the *p*-type character include various metal oxides such as copper oxide (Cu_2O), tin monoxide (SnO) and nickel oxide (NiO).[23–25] Although thin-film transistors (TFTs) based on these materials have shown to exhibit hole mobilities of >1 $cm^2V^{-1}s^{-1}$,[23,24,26] their relatively small bandgap (Cu_2O, SnO)[27–29] yields layers with low transparency, while the high temperature processing that often is required[26,30] renders them incompatible with inexpensive temperature-sensitive substrate materials such as plastic. The use of organic HTLs, such as poly(3,4-ethylenedioxythiophene) polystyrene sulfonate (PEDOT:PSS), has been exploited to address some of these concerns but, in many cases, at the expense of the devices' operating stability.[31–33] A further disadvantage of PEDOT:PSS is its semi-metallic nature, which does not prevent electron flow to the anode; an important efficiency loss process for various organic optoelectronic devices (e.g. OPVs, OLEDs).[4-7] Consequently, there is a continuous demand for wide-bandgap *p*-type semiconductors that combine solubility, optical transparency, high hole mobility and low temperature processing.

It was only recently that the use of CuSCN as the HTL material was shown to yield optoelectronic devices with improved efficiency and lifetime.[7] Despite these promising early results, however, processing of CuSCN is still challenging as it is largely insoluble in the vast majority of common solvents, with sulphur-based solvents being the most effective and widely

studied.[7,34] This limitation restricts CuSCN processing to enclosed and strictly controlled laboratory environments due to the strong odour, although no evidence of CuSCN posing risks to human health are known.[35] Therefore, successful application of CuSCN in the emerging sector of large-area optoelectronics would most certainly require the development of alternative and environmentally-friendly solvents. While reports on alternative organic solvents such as dimethyl sulfoxide do exist, the power conversion efficiencies achieved have been limited (<5%) by the high surface roughness of the resulting CuSCN layer.[36]

Here we report the development of transparent hole-transporting CuSCN layers via spin casting in ambient air from aqueous ammonia [NH_3(aq)] solution [denoted as CuSCN/NH_3(aq)] and their application in *p*-type transistors and high efficiency solar cells. Chemical studies on CuSCN networks,[37–40] which utilized aqueous ammonia as the solvent, and detailed the formation of copper complexes in solution, provided the starting point for this work. The structural, optical and electronic properties of the ammonia-processed CuSCN layers were studied and contrasted with those processed from diethyl sulphide (DES) solution under inert atmosphere. CuSCN transistors processed from NH_3(aq) solution exhibit superior hole transport, as compared to devices processed from DES, with mobility values approaching ~0.1 cm^2/Vs. Incorporation of the ammonia-processed CuSCN as the HTLs in bulk-heterojunction organic and planar organometal halide perovskite solar cells, leads to devices with power conversion efficiency (PCE) of up to 10.7% and 17.5%, respectively. To the best of our knowledge, this is the first demonstration of high performance solution-processed optoelectronic devices where CuSCN is deposited from an aqueous solvent formulation that is inexpensive and compatible with large-area manufacturing.

2. Optical Characterization of CuSCN Solutions and Solid Layers

Following the careful optimization of deposition parameters, highly uniform and ultrathin CuSCN layers were spin-cast on quartz substrates from the aqueous formulation. Typically, CuSCN forms colourless solutions when dissolved in n-alkyl sulphide solvents, such as the DES reference solvent used in this study. On the contrary, a deep blue CuSCN-ammine complex formed when the white CuSCN powder was added and stirred for 1 hour at 50 °C in aqueous ammonia at concentrations of 10-15 mg ml^{-1}. **Figure 1a** shows photographs of the CuSCN/NH_3(aq) and CuSCN/DES solutions. Small quantities of a precipitate were observed in the solutions after 1 hour cooling to ambient temperature (~20 °C). The precipitates are attributed partly to differences in the solubility of CuSCN in aqueous ammonia at lower temperatures and partly to the presence of other copper-based compounds (e.g. copper oxide), which can form as products of redox reactions. For this reason, all solutions were filtered prior to spin coating and thermal annealing at 100 ˚C.

Figure 1b shows the ultraviolet-visible-near-infrared (UV-Vis-NIR) absorbance spectra of the CuSCN-containing solutions together with those of the solid films for comparison. While the absorbance of the CuSCN/DES solution only differed marginally from that of the solvent, significant differences between the NH_3(aq) and CuSCN/NH_3(aq) solutions can be observed due to the complexation chemistry of the latter. Despite this, the ammonia-processed layer exhibits the characteristic CuSCN spectrum, and notably, lacks the absorption features associated with the narrow-bandgap nature of copper oxides. Further consideration of the layer composition leads to the hypothesis that $Cu(SCN)_2$ could only be present as a minority contaminant because the compound rapidly converts to CuSCN in aqueous environment and at elevated temperatures.[41,42] The latter hypothesis is experimentally verified by XPS analysis and will be discussed in **Section 5**.

Figure 1c shows the Tauc plots from which the optical bandgap (E_{OPT}) of the CuSCN/NH_3(aq) processed layer was extracted. Here, $(\alpha h\nu)^n$ is plotted versus incident photon energy ($h\nu$), where α is the absorption coefficient, h is Planck's constant, ν is radiation

frequency, and n is equal to 0.5 for an indirect bandgap semiconductor and 2 for a direct bandgap semiconductor. Linear fits applied to the appropriate regions of the plots yield values of 3.45 (±0.05) and 3.85 (±0.05) eV for the indirect and direct bandgap, respectively. Similarly, spectra from a DES-processed layer yields E_{OPT} values of 3.40 (±0.05) (indirect) and 3.85 (±0.05) eV (direct) (**Figure S1**, *Supporting Information*). These results are consistent with data reported in the literature for CuSCN.[1,20,43–45]

The colour of the solution formed when Cu(I)SCN dissolves in NH_3(aq) is expected to arise from the formation of a Cu^{2+}-ammine complex, which is widely reported to exhibit a characteristic blue colour.[46–48] If this assumption is correct, a Cu(II) compound could be utilized as a source of Cu^{2+} ions for the deposition of CuSCN from an ammonia-based solution where SCN^- ions are also present. To test this hypothesis an experiment to investigate the complexation chemistry of the CuSCN/NH_3(aq) solution was conducted. For this, a mixture of copper(II) oxide (CuO) and ammonium thiocyanate (NH_4SCN) was dissolved in aqueous ammonia at a 1:1 molar ratio; a deep blue saturated solution similar to that observed with the Cu(I)SCN precursor (**Figure 1a**) was formed. **Figure S2** in *Supporting Information* section shows the UV-Vis-NIR transmittance spectra for the ammonia-based solutions containing CuO and NH_4SCN. A broad transmittance peak corresponding to one observed at the 300–500 nm spectral region of the CuSCN/NH_3(aq) solution spectrum was detected for CuO/NH_3(aq), which revealed that the colour observed upon dissolution of CuSCN in aqueous ammonia did indeed originate from an ammine complex containing Cu^{2+} ions. Notably, despite CuO being a low bandgap material, the layers spin-cast from a precursor mixture containing NH_4SCN were optically transparent and exhibited the characteristic CuSCN absorption spectrum. Tauc analysis of the absorption data yielded E_{OPT} values of 3.50 (± 0.05) eV (indirect) and 3.86 (± 0.05) eV (direct) (**Figure S3**). These results verify that CuO and NH_4SCN can indeed be utilized as novel precursors for the synthesis of CuSCN layers from solution phase. Interestingly, one may also argue that the conductivity of the resulting material could, in principle, be controlled

by varying the stoichiometric ratio of the two precursors to generate an excess of Cu or SCN in the semiconductor lattice.[49] However, the latter study is beyond the scope of this work.

3. Surface Morphology of CuSCN Layers Processed From Aqueous Ammonia

CuSCN layers were spin-cast on glass substrates identical to those used for top-gate transistor fabrication, as well as on indium-tin-oxide (ITO) coated glass substrates –the transparent anode electrode widely used in solar cell fabrication– and studied via atomic force microscopy (AFM). **Figure 2a-h** show the surface topography data from eight samples measured with a scan area of 1 μm^2. All CuSCN layers were prepared employing the same conditions used to fabricate the optimized transistors and solar cells which will be discussed in **Sections 7** and **8**. The surface topography of plain glass (**Figure 2a**), glass/ITO (**Figure 2e**), and PEDOT:PSS (**Figure 2f**) spin cast onto glass/ITO (glass/ITO/PEDOT:PSS), are also shown for comparison. Layers processed from CuSCN/NH_3(aq) solutions appear continuous and nanocrystalline (**Figure 2b-c,** and **2g**) with remarkably different surface morphology to layers processed from DES (**Figure 2d**, and **2h**). The latter films (CuSCN/DES) contain elongated crystallites of 50-80 nm in length, while the former (CuSCN/NH_3(aq)) are composed of considerably smaller spherical grains. Using higher magnification (0.5 μm^2) AFM scans the size of the grains for the CuSCN/NH_3(aq) layers could also be evaluated, yielding a diameter of 20–30 nm for films processed from a 10 mg ml^{-1} solution at 800 rpm (conditions used for TFT fabrication), and 10–20 nm for films spin-cast from a 15 mg ml^{-1} solution at 2000 rpm (conditions used in HTL deposition for solar cell fabrication).

Figure 2i shows the surface height histograms extracted from the topography AFM images for CuSCN layers deposited on glass (**Figure 2a–d**). CuSCN layers processed from CuSCN/NH_3(aq) solution (**Figure 2b**) exhibit the smoothest surface topography leading to an

exceptionally low surface root mean squared (RMS) roughness of ~0.4 nm (red curve, **Figure 2i**). On the contrary, CuSCN layers processed from DES show large height variation (pink curve, **Figure 2i**) resulting in significantly higher surface RMS roughness (6.4–7.8 nm). Topographical height distributions were also used to determine the degree of surface planarization achieved when CuSCN/NH_3(aq) solutions were spin-cast onto ITO electrodes. **Figure 2j** shows the height distributions extracted from the AFM data in **Figure 2e–h**. As can be seen, the layers deposited from the CuSCN/NH_3(aq) solution exhibit considerably lower surface roughness (RMS ~ 1.5 nm) relative to the DES-processed film (RMS ~ 8.5 nm). This is an important finding as it demonstrates that CuSCN layers processed from CuSCN/NH_3(aq) are both continuous and help to planarize the rough ITO surface (RMS ~ 3.2 nm). The latter feature may help to reduce the concentration of interfacial defects which could be highly advantageous for the reliable manufacturing of photovoltaic devices.[50,51] Remarkably, the planarization of ITO by the CuSCN/NH_3(aq) processed layer appears to be even superior to PEDOT:PSS, which yields surfaces roughness of ~2.6 nm (red curve, **Figure 2j**).

Since the solubility of CuSCN in NH_3(aq) at room temperature is relatively low, it was possible to spin-cast and thermally anneal (intermittent thermal annealing at 100 °C in air) several layers of CuSCN. This simple approach allowed for careful control of the HTL thickness without affecting the structural quality of the resulting layer. Specifically, AFM data (**Figure S4**) indicate that the multilayer CuSCN HTLs exhibited very similar surface morphology to that measured for single layer systems. Interestingly, a small reduction in the RMS surface roughness of the CuSCN HTL from 1.59 nm, measured for the single layer, to 1.53 nm, for the 3-layer film, was observed (**Figure S4**), further highlighting the applicability of this simple deposition approach.

CuSCN layers processed from DES solutions were consistently found to be substantially thicker than those processed from NH_3(aq) due to the increased viscosity and slower evaporation rate. The exceptionally smooth CuSCN films spin-cast on glass at 2000 rpm from

15 mg ml^{-1} NH_3(aq) solutions were typically 3-5 nm thick, with triple-spin cast layers exhibiting a thickness of ~10 nm. It is thus remarkable to observe the significant planarization effect that such thin layers of CuSCN have on the surface topography of ITO upon deposition (**Figure 2j**). On the contrary, CuSCN layers processed from DES appear to be significantly thicker and in the range of 30-40 nm-thick in agreement with published results.[6-7] Previous reports on the structure of solid CuSCN suggest that nanocrystalline CuSCN films typically contain a mixture of the orthorhombic α-phase and the hexagonal/rhombohedral β-phase when deposited from dipropyl sulfide.[2,6] Hence, we note that there is scope to conduct further structural analysis of CuSCN layers to determine whether the use of aqueous ammonia route has an impact on crystalline phase and orientation, particularly when depositing ultra-thin CuSCN layers onto highly crystalline anode material such as ITO. Preliminary attempts to analyse the microstructure of the CuSCN layers have been unsuccessful primarily due to the ultra-thin nature of the layers.

The ability to reliably deposit continuous CuSCN layers from DES was also investigated. **Figure S5** shows the AFM images for two CuSCN layers deposited using identical conditions, i.e. via spin coating on glass substrates at 800 rpm from 10 mg ml^{-1} DES solutions, followed by thermal annealing at 100 °C in air. Evidently, CuSCN layers, which have been processed following identical experimental conditions, exhibit considerable variations with some films dominated by spherical grains (**Figure S5a**) and others composed of larger, elongated "rice-like" grains (**Figure S5b**). CuSCN/DES films spin-cast in ambient air also exhibit a significantly different crystalline structure to films spin-cast in a nitrogen atmosphere **(Figure 2d)**. While further work is needed to identify the mechanisms underpinning these structural variations, similar observations have been reported in the literature for other inorganic materials, such as copper oxide and ITO, where the atmospheric dependence of thin-film morphology is primarily attributed to the presence of gaseous species that contribute to competing chemical reactions during thermal annealing.[52,53] On the contrary, the surface

morphology of CuSCN/NH_3(aq) layers spin-cast on glass and annealed at 100 °C in ambient air demonstrated high reproducibility. This remarkable feature combined with the elimination of the sulphur-based solvent makes the proposed CuSCN/NH_3(aq) deposition approach a highly promising technology for the growth of HTLs for a wide range of emerging applications.

The deposition and in-situ synthesis of CuSCN layers on glass employing a formulation consisting of CuO and NH_4SCN powders dissolved in NH3(aq), was also investigated. **Figure S6** shows the topography AFM image of the resulting layer after it has been thermally annealed in air. The layers are characterized by a similar surface morphology to those deposited via the CuSCN/NH_3(aq) formulation and contain spherical grains with a diameter in the range 20-30 nm. The surface RMS roughness of the layers is low (~0.6 nm) and comparable to that of those deposited using the CuSCN/NH_3(aq) formulation. Most importantly, the resulting CuSCN films exhibit absorption characteristics identical to layers processed from CuSCN/DES and CuSCN/NH_3(aq) solutions (**Figure S2**), further verifying the successful formation of CuSCN.

4. Density-Functional Theory Calculations

In order to probe the electronic properties of CuSCN we performed Density-Functional Theory (DFT) calculations with the code Quantum Espresso.[54] The details and parameters of the calculations are the same as those used previously for CuSCN.[49,55,56] The DFT values for the lattice vector and energetics of CuSCN are in close agreement with pertinent experimental findings. In particular, the calculations[49] show that the wurtzite phase of bulk CuSCN (the so-called beta phase) is the most stable CuSCN polymorph, as observed. Moreover, the difference between DFT[49] and experimental structural parameters (namely, lattice parameters and atom coordinates within the unit cell of beta-CuSCN) is <1%, which confirms that DFT calculations provide an accurate description of the properties of wurtzite CuSCN.

In this work, we extended the scope of the DFT calculations and also obtained the so-called partial (or projected) densities of states (PDOS). The PDOS results can be combined with

XPS spectra to provide insight into the character of the electronic states within the valence band of the material. In this respect, PDOS plots show that the valence band of CuSCN is dominated by Cu-related states, whereas the conduction band shows significant contributions from the SCN groups, in agreement with other DFT studies.[1] More details on the fine structure of PDOS and related XPS spectra are given in the following section.

5. Elemental Composition, Chemical Bonding and Density of States by XPS

The chemical and electronic properties of CuSCN layers processed from CuSCN/DES and CuSCN/NH_3 were investigated using XPS. Survey spectra of both samples show all expected core levels as well as a small contribution from the silicon (Si) substrate (**Figure S7**). Core level spectra collected for the CuSCN layers processed from DES (**Figure S8)** and NH_3(aq) (**Figure S9**) solutions were analysed in order to investigate the chemical environments present on the layer surfaces. All binding energy (BE) positions stated in the following discussion are those of CuSCN/DES. Values for layers processed from CuSCN/NH_3(aq) differ only slightly and are within the uncertainty associated with the measurement (see **Table S1**). In both cases the main Cu 2*p* core line is at a BE of 932.6 eV, which can be assigned to Cu^{1+} in CuSCN. A slight asymmetry (represented by an additional feature denoted with an asterisk in **Figures S8** and **S9**) is observed for both samples. The absence of satellite features for the CuSCN/DES film, which are typical for Cu in the 2+ oxidation state, excludes this asymmetry stemming from Cu^{2+} species (**Figure S10**), in agreement with previous reports.[57] Furthermore, asymmetry due to the presence of either CuO or Cu_2O can be excluded, as the O 1*s* core level for both samples does not show any features corresponding to these compounds (**Figure S11**), which would appear at BEs of 529.6 and 530.5 eV, respectively.[58] The film deposited from CuSCN/NH_3(aq) solution shows a further peak at 934.9 eV, which is attributed to the presence of $CuSO_4$.[59] This is further confirmed by a strong signal from S-O environments in both the O 1*s* core level at

531.9 eV and the S 2*p* core level at 168.8 eV.[60] In comparison, this feature is very small in the S 2*p* spectrum of the DES deposited film. Besides the main peak in the S 2*p* core level at 163.4 eV, which corresponds to CuSCN, an additional small contribution at lower BE (162.6 eV) is found, which could stem from either C-S or Cu-S environments.[61] The C 1*s* core levels for both samples are dominated by a peak at 286.0 eV, corresponding to CuSCN, and show further peaks at 285.0 eV and 290.1 eV attributed to adventitious carbon and O-C-N (e.g. similar to biuret) environments, respectively. The sample deposited from DES solutions shows a further peak at a low BE of 284.5 eV most likely stemming from C-S environments. Finally, the N 1*s* core level shows the main CuSCN peak at 398.5 eV with both samples also exhibiting a feature at 399.8 eV assigned to N-H environments. The NH_3(aq) processed CuSCN layer has a further low intensity peak at 399.1 eV assigned to a minor contribution from C-N environments. Quantitative analysis of the peak fits was used to investigate the elemental ratios present in CuSCN, which are summarized in **Table S2**. Only peaks attributed to CuSCN (marked with an asterisk in **Table S1**) were used for the quantification. Within the accuracy of the quantification (±0.5%) the S:C:N ratios are 1:1:1. An excess of Cu on the surface compared to CuSCN is found, in particular for the CuSCN/NH_3(aq) processed sample, which is most likely due to the overlap of Cu 2*p* signals from different Cu^{1+} environments as observed in the S, C, and N core levels, which cannot be resolved in XPS due to negligible chemical shifts.

In addition to core level spectra, the valence band (VB) spectra of both samples were collected using XPS (**Figure 3**). A clear shift of the VB maximum VB_{max} to higher BE relative to the Fermi energy (E_F) is visible in the CuSCN/NH_3(aq) processed layers (**Figure 3a**). From linear fits to the VB onset the separation was found to be 0.8 eV for CuSCN/DES and 1.2 eV for films processed from CuSCN/NH_3(aq). In order to analyse the orbital contributions to the valence bands, experimental data were compared to theoretical calculations based on results discussed in **Section 4**. To take into account experimental considerations, theoretically derived partial densities of states (PDOS) of CuSCN were corrected using one electron atomic cross

sections from Yeh and Lindau[62] to account for differences in signal intensities. A Gaussian broadening of 300 meV was applied, comparable to the minimum experimental broadening at E_F (**Figure S12**). The total DOS resulting from the present calculations can then be directly compared to the spectroscopy results, with both experimental and theoretical results aligned to the position of the main Cu 3*d* peak of CuSCN/DES. One previous account of a valence band spectrum of CuSCN measured by XPS and compared to calculated DOS exists, however, the energy resolution of these measurements did not allow for an in depth analysis of the VB features and the assignment of related contributions.[1] Excellent agreement is found between experiment and theory, in particular concerning the number of features and their energy positions (**Figure 3b**). Five major contributions to the VB can be identified. The first feature located between 2 and 4 eV is dominated by Cu 3*d* states with some mixing from Cu 3*p* and S 3*p* states at the very top of the VB. The second feature (4-6 eV) is also dominated by Cu 3*d* states but the influence of both Cu 3*p* and S 3*p* states is increasing. The third feature (6-8 eV) is dominated by Cu 3*p* mixed with S 3*p* states, while the fourth (8-9 eV) and fifth (9-11 eV) features show an additional contribution from N 2*s* states. C states contribute a non-significant amount to the valence states with only a small contribution of C 2*s* states found in the fifth feature. Comparatively, the relative intensities of the second and third features are enhanced in the CuSCN/NH_3(aq) sample.

6. Environmental Stability of CuSCN Layers

Air photoemission spectroscopy (APS) and Kelvin probe (KP) techniques were used to further study the electronic energy levels of CuSCN. The APS spectra obtained from CuSCN layers processed from CuSCN/NH_3(aq) and DES on ITO-coated glass substrates were analysed to extract the valence band maximum (VB_{max}) energy. Obtained results indicated that VB_{max} is independent of the solvent used to within ±0.05 eV, an error attributed to the measurement

resolution. By measuring sets of three CuSCN samples deposited from NH_3(aq) and DES, the VB_{max} energy of CuSCN was found to be -5.36 (±0.05) and -5.40 (±0.05) eV. The APS data further confirms that CuSCN is chemically stable even when processed in environments with high oxygen and water content. On the basis of these findings, we conclude that the material is compatible with the aqueous synthetic/deposition route proposed.

Next, the environmental stability of CuSCN HTLs was examined using the KP system by monitoring temporal variations in the Fermi energy level following exposure to ambient air. At time (t) = 0 s, which corresponds to the time when the sample was transferred from the fabrication environment to the sample chamber, E_F for NH_3(aq) and DES-processed CuSCN layers were 5.07 and 5.23 eV, respectively. Notably, the value of E_F for both samples was found to increase as compared to that recorded at t = 0 s following 1 hour of ambient air exposure, reaching values of 5.15 eV (NH_3(aq)) and 5.39 eV (DES). This characteristic energy shift towards the VB_{max} was attributed to atmospheric p-doping.[6] However, as discussed previously in **Section 5**, the high resolution valence band spectra indicated that the E_F is ~0.8 eV above the VB_{max} in CuSCN layers processed from DES, and ~1.2 eV above the VB_{max} in CuSCN layers processed from NH_3(aq) solutions. To this end, the high vacuum environment used during XPS measurements would most likely lead to oxygen and water desorption and as such yield a more realistic E_F. Therefore, the smaller energy difference determined from the KP and APS data is attributed to a reversible and unintentional *p*-doping of CuSCN that arises from sample exposure to ambient air prior to and during measurements. Encouragingly, no change in the VB_{max} energy of CuSCN layers, evaluated by APS, was observed following a 7-day period of ambient air exposure. This result verifies the chemical stability of CuSCN and highlights its potential as a HTL material.

7. CuSCN Transistors Processed from Aqueous Ammonia Solutions

The charge transport properties of CuSCN layers processed from NH_3(aq) and DES were investigated in top-gate, bottom-contact (TG-BC) transistors using poly(vinylidenefluoride-trifluoroethylene-chlorofluoroethylene) [P(VDF-TrFE-CFE)] as the high-k polymer dielectric (**Figure 4**, inset). The transfer characteristics (i.e. source-drain current (I_D) versus gate voltage (V_G)) of the transistors were recorded at two drain voltages (V_D) corresponding to the linear (lin) and saturation (sat) operating regimes. Electrical characterization of the transistors was carried out in a nitrogen-filled glovebox to avoid unwanted exposure of the CuSCN layers to atmospheric oxidants. **Figure 4** shows the transfer curves measured in saturation for two CuSCN transistors, one processed from NH_3(aq) and one from DES, for comparison. The output characteristics and the linear regime transfer curves corresponding to the device data in **Figure 4** are presented in **Figure S13** in *Supporting Information*. The channel length (L) and width (W) for both transistors were 30 and 1000 µm, respectively. Both transistors exhibit clear hole-transporting characteristics with low operating voltages (~|10| V), small hysteresis and clear channel current saturation. Encouragingly, CuSCN layers processed from NH_3(aq) exhibit improved hole transport as compared to DES-processed layers, manifested as increased channel current (**Figure 4**). Analysis of the data obtained from the NH_3(aq)-processed CuSCN devices yielded a mean and a maximum hole mobility of 0.05 and 0.07 $cm^2V^{-1}s^{-1}$, respectively. A comparatively lower mean saturation mobility of 0.01 $cm^2V^{-1}s^{-1}$ was extracted for the DES-processed CuSCN transistors (**Table 1**).

The subthreshold swing (SS) was also calculated from the linear transfer characteristics for each CuSCN transistor and used to extract the corresponding trap concentrations.[63] Surprisingly, and despite the improved hole transport observed in NH_3(aq)-processed CuSCN TFTs, the SS values obtained were approximately 1 V dec^{-1} higher than those extracted from devices processed from DES (typically 1–2 V dec^{-1}). Corresponding analysis yields trap concentration in the range of 4.2–6.3x10^{13} cm^{-2} for CuSCN devices processed from NH_3(aq), as compared to 2.1–4.2x10^{13} cm^{-2} for DES-processed transistors. These finding highlights the

potential for further device optimization through interfacial engineering. Finally, functional CuSCN transistors were also realized from CuO/NH_4SCN precursor solution (**Figure S14**). Although the resulting devices exhibited significantly lower hole mobility (~0.002 $cm^2V^{-1}s^{-1}$), we note that process optimization is anticipated to lead to performance improvement. Nevertheless, the result demonstrates the generic nature of the synthetic route proposed here for the growth of CuSCN at low temperature.

8. Organic and Organometal Halide Perovskite Photovoltaic Cells with CuSCN Hole-Transport Layers Processed from Aqueous Solutions in Air

Finally, the suitability of NH_3(aq)-processed CuSCN for application as HTLs in organic bulk-heterojunction (BHJ) and organometal halide perovskite solar cells was investigated. First, normal architecture single-stack organic photovoltaic (OPV) devices were fabricated using poly[4,8-bis(5-(2-ethylhexyl)thiophen-2-yl)benzo[1,2-b:4,5-b′]dithiophene-alt-3-fluorothieno[3,4-b]thiophene-2-carboxylate] (PTB7-Th) as the donor and [6,6]-phenyl-C_{71}-butyric acid methyl ester ($PC_{70}BM$) as the acceptor material (**Figure 5a**) materials. **Figures 5b** and **5c** show the standard device architecture employed and the corresponding material energetics, respectively. For this type of cell, bathocuproine (BCP) was employed as the electron transport layer (ETL) and was deposited via thermal sublimation. **Figure 5d** displays the current density-voltage (J-V) characteristics of three identical solar cells that differ only by the type of the HTL employed, namely; CuSCN/NH_3(aq), CuSCN/DES, and PEDOT:PSS. The extracted cell parameters are summarized in **Table 2**. Evidently, devices based on CuSCN/NH_3(aq) demonstrate enhanced performance with respect to cells made with PEDOT:PSS and CuSCN/DES HTLs. Notably, compared to PEDOT:PSS the bilayer CuSCN/NH_3(aq)-containing OPV cells yield higher short circuit current (J_{SC}), open circuit voltage (V_{OC}) and fill factor (FF), resulting in cells with an average power conversion

efficiency (PCE) of 10.01% (measured over eight devices) and a maximum value of 10.7%. Remarkably, the latter PCE value is higher than those measured for the best-performing inverted cell (PCE = 10.2%) prepared from the same active layer (see **Figure 5e**). The PCE value of 10.7% represents one of the highest, if not the highest, values achieved to date in non-inverted PTB7-Th:$PC_{70}BM$-based OPVs. Furthermore, and as evident from **Table 2,** CuSCN/NH_3(aq) HTLs processed via single, double and triple spin-coating steps all yield OPVs with average PCE values (>9.25%) above that of PEDOT:PSS (9.1%) clearly demonstrating the ability to realize high-performance OPVs using CuSCN HTLs processed from an aqueous solution in air.

Previous reports have attributed the superior performance of OPVs with CuSCN HTLs, as compared to PEDOT:PSS, to a combination of an increase in V_{OC} due to the deeper VB_{MAX} energy of CuSCN,[7,10] and an enhanced J_{SC} due to decreased parasitic absorption by the HTL.[7,8] Additionally, the low electron affinity of CuSCN (-1.5 eV, see **Figure 5c**) suppresses the dark minority carrier injection from the anode to the active layer (and vice versa), which is manifested as reduced reverse dark saturation current when compared to PEDOT:PSS-based cells (**Figure 5f**). Furthermore, the ultra-smooth surface of the CuSCN/NH_3(aq) HTLs (**Figure 2g** and **2j**) is believed to lead to improved electrical contact with the active layer, which in turn translates to a notable increase in the FF from 0.60 for PEDOT:PSS-based cells to 0.63 for CuSCN/NH_3(aq)-based cells. Conversely, the FF for cells with CuSCN/DES HTLs is found to be lower than that for PEDOT:PSS-containing OPVs (**Table 2**). We attribute this to the high surface roughness of CuSCN/DES layers (**Figure 2h** and **2j**), which could well lead to a poor interfacial contact between CuSCN and the PTB7-Th:$PC_{70}BM$ blend, with adverse effects on the charge extraction efficiency.

The effect of CuSCN/NH_3(aq) on the operating stability of the OPV cells was also briefly investigated. Standard architecture PTB7-Th:$PC_{70}BM$-based cells based on

PEDOT:PSS HTLs are known to suffer from rapid performance degradation due to the inability of PEDOT:PSS to filter UV radiation, which has been shown to lead to the degradation of the active layer due to morphological changes.[64,65] **Figure 5g** shows the preliminary stability data for two PTB7-Th:$PC_{70}BM$ based OPV cells with PEDOT:PSS (solid symbols) and CuSCN/NH_3(aq) (open symbols) as the HTL. Cells with PEDOT:PSS show a 35% drop in the PCE following a 10 minute exposure to constant AM1.5 illumination. In contrast, cells made with CuSCN/NH_3(aq) undergo only a 15% drop in PCE for the same illumination period, which is primarily attributed to the FF remaining almost unaffected by illumination in the devices containing CuSCN/NH_3(aq) HTLs (**Figure 5g**), and is due to the strong UV filtering property of CuSCN as evident from the UV absorption peak in **Figure 1b**. Although preliminary, the results indicate that OPVs with NH_3(aq)–processed CuSCN HTLs could potentially outperform those based on commercially available HTL material technologies.

Finally, the applicability of the aqueous–processed CuSCN HTLs[66,67] to organometal halide perovskite photovoltaic cells[68–71] was also investigated. The perovskite precursor solution was prepared using a solvent blend of dimethyl sulfoxide and gamma butyrolactone, which is a less hazardous alternative to some precursor solvents, such as N,N-dimethylformamide, reported in the literature.[72] **Figure 6a-b** shows the device architecture and the corresponding material energetics, while **Figure 6c** displays the J-V characteristics obtained using a 50 mV/s scanning rate, for the optimized organometal halide perovskite solar cells with CuSCN/NH_3(aq) and PEDOT:PSS as HTLs. The PCE for the PEDOT:PSS-based cell is 13.6%, a reasonable value compared with literature using similar methods.[73] Replacing PEDOT:PSS with CuSCN/NH_3(aq) as HTL, however, results in a significant increase of PCE to 17.5%. The performance enhancement is attributed to two main effects. Firstly, to a V_{OC} increase by 200 mV from 0.9 V for PEDOT:PSS to 1.1 V for CuSCN/NH_3(aq), which indicates improved energetic alignment between the HTL and

$CH_3NH_3PbI_3$ (**Figure 6b**), and secondly to an increased J_{SC} (22.7 mA/cm^2). However, we note that this improvement is accompanied by a slight drop in the FF from 0.73 for PEDOT:PSS, to 0.71 for the CuSCN/NH_3(aq)-based cells. Generally speaking, the relatively low V_{OC} represents the major hurdle for achieving high PCE in planar inverted perovskite cells (HTL on bottom, ETL on top), particularly using PEDOT:PSS as the HTL. It is therefore notable that the V_{OC} value of 1.1 V achieved here for the CuSCN/NH_3(aq)-based perovskite cells is comparable to values achieved in some highly efficient invert-structured cells using poly(triaryl amine) (PTAA) or nickel oxide (NiO_x) as HTLs.[74,75] In contrast, replacing PEDOT:PSS with CuSCN/DES as HTL resulted in a significantly lower maximum PCE of 10.2%. The J-V characteristics of a $CH_3NH_3PbI_3$ solar cell based on a CuSCN/DES HTL is presented in **Figure S15** in *Supporting Information*. We note that this experiment was conducted at a later date, where the best PEDOT:PSS-based reference cell yielded a PCE of 13.9%. The inferior performance of the CuSCN/DES-based devices is attributed to non-uniformities in the HTL morphology, which is likely to have a significant negative impact on the perovskite crystallization process, and result in increased shunting pathways and interfacial current losses. This is indicated by the lower FF (0.63-0.71) and J_{SC} (10.5-14.2 mA cm^{-2}) observed in cells containing CuSCN/DES HTLs.

Furthermore, **Figure S16** (*Supporting Information*) shows that solar cells based on CuSCN/NH_3(aq) HTLs exhibit better operating stability over a 3h period of constant 1-sun simulated solar illumination compared to identical devices containing PEDOT:PSS and CuSCN/DES HTLs. In this preliminary test, PCE of the CuSCN/NH_3(aq)-based cell dropped to 99.5% of its original value during the first 1 hr of illumination, and decreased steadily to 91.1% of the initial efficiency after 2 h. Meanwhile, PCE of the PEDOT:PSS-based device fluctuated over time and decreased to 91.0% of its original value over the 3 h period, and PCE of the CuSCN/DES-based device deteriorated rapidly to 82.7% of its original value during the same time period. The poor operating stability of the CuSCN/DES-based solar

cell in a nitrogen atmosphere supports our hypothesis about the crystallization of $CH_3NH_3PbI_3$ on CuSCN/DES, because the formation of a disordered and defective HTL-perovskite interface is likely to be a major cause of cell instability. Further research is needed to experimentally determine the physical mechanisms that underpin these differences in operating stability, but that is beyond the scope of this work. Importantly, while the use of aqueous ammonia may raise concerns about residual water traces existing in the HTL film, the superior performance and stability of solar cells containing CuSCN/NH_3(aq) HTLs reveal no evidence of the aqueous processing solvent having a detrimental effect on the perovskite layer formation or device function. Therefore, we conclude that thermally annealing of the as-spun CuSCN/NH_3(aq) layers at 150 ˚C for 15 minutes is sufficient to fully evaporate aqueous ammonia, and obtain an anhydrous HTL that functions extremely well in perovskite solar cells.

9. Conclusion

In conclusion, we have demonstrated high performance *p*-channel transistors, organic solar cells and organometal halide perovskite solar cells based on CuSCN hole-transport layers processed from an aqueous ammonia-based precursor solution in ambient air. Various material characterization techniques confirmed that CuSCN layers processed from NH_3(aq) solutions exhibited high compositional purity, exceptional surface uniformity, and superior substrate planarization properties relative to CuSCN layers processed from DES as well as PEDOT:PSS. Furthermore, the improved hole mobilities observed in NH_3(aq)-processed CuSCN transistors, as compared to DES-processed devices, indicated that the proposed deposition route yields CuSCN with enhanced hole transport characteristics. Consequently, PTB7-Th:$PC_{70}BM$ cells based on NH_3-processed CuSCN HTLs exhibit improved PCE (10.7%), J_{SC} (21.1 mA/cm^2), FF (0.63) and high V_{OC} (0.80 V) as compared to PEDOT:PSS-based devices. Surprisingly, the

maximum PCE value of 10.7% is achieved in cells with non-inverted architecture. Lastly, the applicability of the aqueous-processed CuSCN HTL was extended to organometal halide perovskite photovoltaic cells for which a maximum PCE of 17.5% was achieved – a remarkably higher value than that achieved in PEDOT:PSS-based cells (13.6%). These results demonstrate the enormous potential of CuSCN for a wide range of opto/electronic applications as it can now be solution-processed from an environmentally-friendly aqueous precursor formulation at low temperatures and in atmospheric air without any special precautions.

10. Experimental Section

***CuSCN Preparation*:** Solutions were prepared by dissolving CuSCN (99%, Sigma-Aldrich) in diethyl sulfide (Sigma-Aldrich, 98%) and aqueous ammonia (50% v/v, Alfa Aesar) at concentrations of 10 mg ml^{-1}, 15 mg ml^{-1} and 25 mg ml^{-1}. After stirring the solutions at 50 °C for 1 hour, the solutions were left to stand in a room temperature environment for an additional hour until the system reached thermodynamic equilibrium. CuSCN/NH_3 solutions were filtered using a hydrophilic filter prior to thin-film deposition. In order to study the complexation chemistry of the CuSCN-ammine complex, copper(II) oxide (CuO, 99%, Sigma-Aldrich) and ammonium thiocyanate (NH_4SCN, 99%, Sigma-Aldrich) were dissolved at a total concentration of 10 mg ml^{-1} (1:1 molar ratio) in aqueous ammonia. CuSCN solutions were pH tested prior to ambient air deposition as the literature reports that cyanide compounds are detected in aqueous thiocyanate solutions under acidic conditions, but are not observed under alkaline conditions, particularly when the pH exceeds 10.6.[76] The organic DES solvent and the CuSCN/DES solutions were found to be neutral with a pH of 7. In contrast, the aqueous 7.0 M ammonium hydroxide solvent utilized in this experiment was found to be strongly alkaline, with a pH of 12. While the dark colour of the CuSCN/NH_3(aq) solution limited the precision of

the pH indicator test, a pH in the range 11–13 was revealed, confirming the presence of a strong alkaline environment, which tends to inhibit the formation of cyanide compounds. Therefore, the ammonia-based CuSCN solutions were considered suitable for ambient air processing in small volumes. However, further studies to verify these results should be performed prior to proceeding with large-scale production. Notably, in contrast to the CuSCN solutions, the PEDOT:PSS dispersion is strongly acidic and has a pH of 1.5–2.5 as specified by the supplier.

Thin-Film Deposition: Substrates were solvent-cleaned prior to thin-film deposition by a sequential ultrasonication procedure: an aqueous solution of Decon 90, deionized water, acetone, and isopropanol. Next, the samples were dried using a nitrogen flow and UV-ozone treated; the latter step was essential to create a hydrophilic surface for the deposition of CuSCN from aqueous ammonia. 10 mg ml^{-1}, 15 mg ml^{-1} and 25 mg ml^{-1} CuSCN solutions were spin-cast at room temperature in ambient air or nitrogen atmosphere environments. Higher spin speeds of 2000 rpm and 2500 rpm were used to deposit thin-films of greater uniformity for photovoltaic applications, while a slower spin speed of 800 rpm was utilized to spin-cast thicker films for TFT applications. DES-based CuSCN solutions were spun for 60 s, while the ammonia-based solutions were spun for a shorter time period of 20 s due to the low boiling point of ammonium hydroxide, typically defined in the literature as 36 °C for a 30% v/v solution. As-spun films were annealed at 100 ˚C for 10 minutes on hotplates in the respective environments. Atmospheric humidity levels were monitored throughout the experiment as 30-40% in ambient air and 0–5 ppm in the nitrogen-filled glovebox.

Ultraviolet – visible – near-infrared (UV-Vis-NIR) spectroscopy**:** The samples were measured using a Shimadzu UV-2600 spectrophotometer equipped with an ISR-2600Plus integrating sphere. Transmittance spectra were recorded in the 220–1400 nm wavelength range, and the absorbance was calculated from the logarithm (base ten) of the spectral data. Liquid samples

were placed in sealed quartz cuvettes during the measurement procedure, while CuSCN thin-films were spin-cast at 2000 rpm on solvent-cleaned quartz substrates. Additionally, the reflectance spectra of thin-films were recorded over an identical range of wavelengths in order to determine the optical bandgap of the semiconductor using Tauc analysis. All data were analysed using Origin software.

Atomic force microscopy (AFM): The surface morphology of films spin-cast on glass and ITO was studied using tapping-mode AFM – an Agilent 5500AFM system. The cantilever had an approximate resonant frequency of 270 kHz and a force constant of 40 N m^{-1}, and the topography and phase data were recorded using PicoView scanning probe microscopy control software. Information on material crystallinity, grain size, and thin-film uniformity were determined from the analysis of 1 μm^2 and 10 μm^2 AFM images using Gwyddion software; all surface height data were extracted from AFM images at an identical resolution in order to generate representative distributions.

X-ray photoelectron spectroscopy (XPS): The surface of CuSCN films spin-cast on solvent-cleaned heavily doped Si^{++} substrates was characterized using X-ray photoelectron spectroscopy (XPS). The spectra were recorded on a Thermo Scientific K-Alpha$^+$ spectrometer operating at a base pressure of $2x10^{-9}$ mbar. This system incorporates a monochromated, microfocused Al Kα X-ray source (hν = 1486.6 eV) and a 180° double focusing hemispherical analyser with a 2D detector. The X-ray source was operated at 6 mA emission current and 12 kV anode bias. Data were collected at pass energies of 200 eV for survey, 20 eV for core level, and 15 eV for valence band spectra using an X-ray spot size of 400 μm^2. Samples were mounted using carbon loaded conductive tape, and in addition, a flood gun was used to minimize sample charging. All spectra were aligned using the C 1*s* contribution of adventitious carbon at 285.0 eV. All data were analysed using the Avantage software package.

Kelvin Probe (KP) measurements and air photoemission spectroscopy (APS): The Fermi level and valence band maximum in CuSCN films were determined using KP contact potential difference measurements and APS, respectively. Films were spin-cast on solvent-cleaned ITO-coated glass substrates and full coverage of the conductive ITO was ensured. The KP-APS set-up comprised of a KP Technology SKP5050 Scanning Kelvin Probe and an APS02 Air Photoemission System. The contact potential difference of each semiconductor thin-film was measured relative to that of a polished silver reference sample, and hence, the Fermi level was calculated with respect to the work function of the reference metal. The KP measurements were made immediately following the transfer of CuSCN films from the fabrication environment to the sample chamber of the instrument, and data recording timescales were adjusted accordingly to monitor temporal variations in the Fermi level. The energy corresponding to the valence band edge was extracted from APS data, where each sample was exposed to ultraviolet radiation of wavelengths in the 200–300 nm range, and the photoemission signal from the layer surface was recorded as a function of wavelength.

Transistor Fabrication and Characterization: Transistors with a staggered top-gate, bottom-contact (TG-BC) architecture were fabricated by spin-casting the 10 mg ml^{-1} CuSCN precursor solutions at 800 rpm on glass substrates. 40 nm-thick gold source-drain contacts (S-D) were thermally evaporated using shadow masks, and subsequently, UV-ozone treated to improve hole-injection into the valence band of CuSCN.[6] Next, CuSCN films were spin-cast and thermally annealed according to procedures detailed above. The high-k relaxor ferroelectric polymer, poly(vinylidenefluoride-trifluoroethylene-chlorofluoroethylene) [P(VDF-TrFE-CFE)], was spin-cast on CuSCN as the dielectric and annealed at 60 ˚C for 1 hour. Finally, 40 nm-thick aluminium gate electrodes were thermally evaporated using shadow masks in high vacuum to complete the device fabrication. Transistors were characterized at room temperature

in a nitrogen-filled glovebox, using an Agilent B2902A parameter analyser. Saturation regime hole mobility (μ_{sat}) values were calculated using the standard gradual channel approximation transistor model:

$$\mu_{sat} = \frac{L}{WC_{ins}}\left[\frac{\partial^2 I_{D(sat)}}{\partial V_G^2}\right] \quad (1)$$

where C_{ins} is the geometric capacitance of the gate dielectric, L is the channel length, and W is the channel width.

Photovoltaic Cell Fabrication and Characterization: Normal structure organic solar cells were fabricated using PEDOT:PSS and CuSCN as the HTLs. Specifically, as-received aqueous dispersion of PEDOT:PSS (CLEVIOS PH 1000, Heraeus) was spin-cast on ITO-coated glass at 7000 rpm and annealed at 140 °C for 20 minutes as a reference HTL film. NH_3(aq)-processed CuSCN HTLs were spin-cast at 2000 rpm from 15 mg ml^{-1} solutions and annealed at 100 °C in ambient air. Optimized DES-processed CuSCN layers were spin-cast at 3500 rpm from 25 mg ml^{-1} solutions and annealed at 100 °C in an N_2 atmosphere. For the inverted structure solar cells, zinc acetate (99.99%, Sigma-Aldrich) was dissolved at 110 mg/ml in 2-methoxyetahanol (anhydrous, 99.8%, Sigma-Aldrich) containing 3% ethanolamine (99.5%, Sigma-Aldrich), and was subsequently spin-cast on ITO-coated glass at 4000 rpm and then annealed at 150 °C for 20 minutes in air. Next, the BHJ active layer composed of a 1.5:1 weight ratio blend of PTB7-Th (Ossila) and $PC_{70}BM$ (Solenne BV), and 3% of the 1,8-diiodooctane (DIO) additive, was spin-cast at 1750 rpm from a 20 mg ml^{-1} chlorobenzene solution. A methanol rinse was performed at 4000 rpm immediately after deposition of the active layer. The active layer was dried by placing the samples under a high vacuum (10^{-7} mbar) overnight inside the evaporator chamber, after which the cells were completed by the thermal evaporation of a 10 nm-thick layer of bathocuproine (BCP) followed by a 70 nm-thick layer of Al electrode for the normal structure solar cells, and a 10 nm-thick layer of molybdenum trioxide (MoO_3, 99.97%, Sigma-

Aldrich) followed by a 70 nm-thick layer of silver electrode for the inverted structure solar cells, through shadow masks. The J-V characteristics of the cells were measured in an inert atmosphere using a Keithley 2400 source-meter. The AM1.5 illumination was provided by a Sciencetech Inc. Solar Simulator SF300-A, with an active area of 5 mm^2 defined by a metal stencil mask.

The organometal halide perovskite solar cells were fabricated on ITO-coated glass substrates using CuSCN and PEDOT:PSS as the HTLs. CuSCN was processed from a NH_3(aq) solution (15 mg ml^{-1}) via spin-casting at 3500 rpm and annealed at 150 °C in ambient air. In contrast to the CuSCN deposition process outlined for the OPV cell fabrication, a higher spin speed was required due to the smaller area of substrates used in perovskite cell fabrication, while a higher annealing temperature was utilized to ensure that the aqueous solvent was evaporated entirely from the CuSCN layer. PEDOT:PSS was spin-cast at 3500 rpm for 45 seconds, and annealed at 150 °C for 10 minutes. Prior to HTL deposition, the substrates were treated by oxygen plasma for 8 minutes. The precursor solution of organometal halide perovskite was prepared by co-dissolving 1.25 M lead iodide (PbI_2, 99.5%, Sigma Aldrich) and methylammonium iodide (MAI, Dyesol) in a mixed solvent of gamma-butyrolactone and dimethyl sulfoxide (Sigma Aldrich, 7:3 by volume). The solution was stirred for 2 hours and filtered before use. The precursor solution was first first spun at 500 rpm for 5 s, and then at 2000 rpm for 20 s. 50 ml of toluene was instantly dripped onto the film at the end of the second stage of spin-casting and followed by a final spin at 4000 rpm for 20 s. The as-deposited semitransparent films were then transferred onto a hotplate and annealed at 100 °C for 10 minutes. Electron transport layers (ETLs) composed of the phenyl-C_{61}-butyricacid methylester ($PC_{60}BM$, Ossila, UK) were deposited onto the perovskite layer via spin-casting from a chlorobenzene solution (18 mg ml^{-1}) at 1300 rpm for 60 s. Finally, the devices were completed by thermally evaporating a 0.7 nm-thick layer of lithium fluoride (LiF) and 100 nm of silver (Ag) onto $PC_{60}BM$ under high vacuum. With the exception of CuSCN, all other solution

processing steps were performed inside a nitrogen-filled glovebox. J-V characteristics were recorded with a Keithley 2400 source-meter. The cells were illuminated by an AM1.5 xenon lamp solar simulator (Oriel Instruments). The intensity was adjusted to 1 sun by changing the working current, which was monitored using a calibrated Si reference photodiode. All devices were stored in dark prior to characterization and were measured in a nitrogen-filled chamber.

Supporting Information

Supporting Information is available from the Wiley Online Library or from the authors.

Acknowledgements

N.W. Y-H.L, H.F., and T.D.A. are grateful to the to the European Research Council (ERC) AMPRO grant number 280221, and the Engineering and Physical Sciences Research Council (EPSRC) grant number EP/L504786/1, for financial support. D.J.P. acknowledges support from the Royal Society (UF100105) and (UF150693). D.J.P. and A.R. acknowledge support from the EPSRC (EP/M013839/1 and EP/M028291/1). M.A.M. and T.D. are grateful for support through the EPSRC Centre for Doctoral Training in Plastic Electronics EP/L016702/1 and the Stephen and Anna Hui Scholarship (Imperial College London).

References

[1] J. E. Jaffe, T. C. Kaspar, T. C. Droubay, T. Varga, M. E. Bowden, G. J. Exarhos, *J. Phys. Chem. C* **2010**, *114*, 9111.

[2] P. Pattanasattayavong, N. Yaacobi-Gross, K. Zhao, G. O. N. Ndjawa, J. Li, F. Yan, B. C. O'Regan, A. Amassian, T. D. Anthopoulos, *Adv. Mater.* **2013**, *25*, 1504.

[3] P. Pattanasattayavong, A. D. Mottram, F. Yan, T. D. Anthopoulos, *Adv. Funct. Mater.* **2015**, *25*, 6802.

[4] L. Petti, P. Pattanasattayavong, Y. Lin, N. Münzenrieder, G. Cantarella, N. Yaacobi-, F. Yan, G. Tröster, T. D. Anthopoulos, *Appl. Phys. Lett.* **2017**, *110*, 113504.

[5] N. Wijeyasinghe, T. D. Anthopoulos, *Semicond. Sci. Technol.* **2015**, *30*, 104002.

[6] P. Pattanasattayavong, G. O. N. Ndjawa, K. Zhao, K. W. Chou, N. Yaacobi-Gross, B. C. O'Regan, A. Amassian, T. D. Anthopoulos, *Chem. Commun.* **2013**, *49*, 4154.

[7] N. Yaacobi-Gross, N. D. Treat, P. Pattanasattayavong, H. Faber, A. K. Perumal, N. Stingelin, D. D. C. Bradley, P. N. Stavrinou, M. Heeney, T. D. Anthopoulos, *Adv. Energy Mater.* **2015**, *5*, 1401529.

[8] N. D. Treat, N. Yaacobi-Gross, H. Faber, A. K. Perumal, D. D. C. Bradley, N. Stingelin, T. D. Anthopoulos, *Appl. Phys. Lett.* **2015**, *107*, 013301.

[9] P. Qin, S. Tanaka, S. Ito, N. Tetreault, K. Manabe, H. Nishino, M. K. Nazeeruddin, M. Grätzel, *Nat. Commun.* **2014**, *5*, 3834.

[10] K. Zhao, R. Munir, B. Yan, Y. Yang, T. Kim, A. Amassian, *J. Mater. Chem. A* **2015**, *3*, 20554.

[11] S. Ye, W. Sun, Y. Li, W. Yan, H. Peng, Z. Bian, Z. Liu, C. Huang, *Nano Lett.* **2015**, *15*, 3723.

[12] A. Perumal, H. Faber, N. Yaacobi-Gross, P. Pattanasattayavong, C. Burgess, S. Jha, M. a McLachlan, P. N. Stavrinou, T. D. Anthopoulos, D. D. C. Bradley, *Adv. Mater.* **2015**, *27*, 93.

[13] L.-J. Xu, J.-Y. Wang, X.-F. Zhu, X.-C. Zeng, Z.-N. Chen, *Adv. Funct. Mater.* **2015**, *25*, 3033.

[14] X. Zhang, S. Yoshioka, N. Loew, M. Ihara, In *ECS Transactions 64*; 2014; Vol. 64, pp. 1–13.

[15] S. Yoshioka, T. Mishima, M. Ihara, In *ECS Transactions 50*; 2013; Vol. 50, pp. 33–44.

[16] S. Ito, S. Tanaka, H. Vahlman, H. Nishino, K. Manabe, P. Lund, *ChemPhysChem* **2014**, *15*, 1194.

[17] E. Bacaksiz, S. Aksu, G. Çankaya, S. Yılmaz, İ. Polat, T. Küçükömeroğlu, A. Varilci, *Thin Solid Films* **2011**, *519*, 3679.

[18] S. M. Hatch, J. Briscoe, S. Dunn, *Thin Solid Films* **2013**, *531*, 404.

[19] Y. Selk, T. Yoshida, T. Oekermann, *Thin Solid Films* **2008**, *516*, 7120.

[20] W. Wu, Z. Jin, Z. Hua, Y. Fu, J. Qiu, *Electrochim. Acta* **2005**, *50*, 2343.

[21] B. O'Regan, D. T. Schwartz, S. M. Zakeeruddin, M. Grätzel, *Adv. Mater.* **2000**, *12*, 1263.

[22] C. Chappaz-Gillot, R. Salazar, S. Berson, V. Ivanova, *Electrochim. Acta* **2013**, *110*, 375.

[23] E. Fortunato, V. Figueiredo, P. Barquinha, E. Elamurugu, R. Barros, G. Gonçalves, S.-H. K. Park, C.-S. Hwang, R. Martins, *Appl. Phys. Lett.* **2010**, *96*, 192102.

[24] J. Caraveo-Frescas, P. Nayak, H. Al-Jawhari, D. Granato, U. Schwingenschloegl, H. Alshareef, *ACS Nano* **2013**, *7*, 5160.

[25] M. D. Irwin, D. B. Buchholz, A. W. Hains, R. P. H. Chang, T. J. Marks, *PNAS* **2008**, *105*, 2783.

[26] D. Muñoz-Rojas, M. Jordan, C. Yeoh, A. T. Marin, A. Kursumovic, L. A. Dunlop, D. C. Iza, A. Chen, H. Wang, J. L. MacManus Driscoll, *AIP Adv.* **2012**, *2*, 042179.

[27] S.-Y. Sung, S.-Y. Kim, K.-M. Jo, J.-H. Lee, J.-J. Kim, S.-G. Kim, K.-H. Chai, S. J. Pearton, D. P. Norton, Y.-W. Heo, *Appl. Phys. Lett.* **2010**, *97*, 222109.

[28] Y. Ogo, H. Hiramatsu, K. Nomura, H. Yanagi, T. Kamiya, M. Hirano, H. Hosono, *Appl. Phys. Lett.* **2008**, *93*, 032113.

[29] P. Pattanasattayavong, S. Thomas, G. Adamopoulos, M. A. McLachlan, T. D. Anthopoulos, *Appl. Phys. Lett.* **2013**, *102*, 163505.

[30] S. R. Thomas, P. Pattanasattayavong, T. D. Anthopoulos, *Chem. Soc. Rev.* **2013**, *42*, 6910.

[31] K. Sun, S. Zhang, P. Li, Y. Xia, X. Zhang, D. Du, F. H. Isikgor, J. Ouyang, *J. Mater. Sci. Mater. Electron.* **2015**, *26*, 4438.

[32] A. Garcia, G. C. Welch, E. L. Ratcliff, D. S. Ginley, G. C. Bazan, D. C. Olson, *Adv. Mater.* **2012**, *24*, 5368.

[33] M. P. de Jong, L. J. van IJzendoorn, M. J. A. de Voigt, *Appl. Phys. Lett.* **2000**, *77*, 2255.

[34] G. R. R. A. Kumara, A. Konno, G. K. R. Senadeera, P. V. V Jayaweera, D. B. R. A. De Silva, K. Tennakone, *Sol. Energy Mater. Sol. Cells* **2001**, *69*, 195.

[35] *CLH Report. Proposal for harmonised classification and labelling. Substance name: copper thiocyanate or copper (I) thiocyanate or cuprous thiocyanate*; 2013; Vol. 2008, pp. 1–191.

[36] N. Chaudhary, R. Chaudhary, J. P. Kesari, A. Patra, *Opt. Mater* **2017**, *69*, 367.

[37] K. M. Miller, S. M. McCullough, E. A. Lepekhina, I. J. Thibau, R. D. Pike, X. Li, J. P. Killarney, H. H. Patterson, *Inorg. Chem.* **2011**, *50*, 7239.

[38] A. Blake, N. Champness, M. Crew, L. Hanton, S. Parsons, M. Schroeder, *J. Chem. Soc. Dalt. Trans.* **1998**, 1533.

[39] A. Blake, N. Brooks, N. Champness, C. Marcello, L. Hanton, P. Hubberstey, S. Parsons, M. Schröder, *J. Chem. Soc. Dalt. Trans.* **1999**, 2813.

[40] G. Ayala, T. A. Tronic, R. D. Pike, *Polyhedron* **2016**, *115*, 257.

[41] D. Tudela, *J. Chem. Educ.* **1993**, *70*, 174.

[42] J. Hunter, W. Massie, J. Meiklejohn, J. Reid, *Inorg. Nucl. Chem. Lett.* **1969**, *5*, 1.

[43] K. Tennakone, A. H. Jayatissa, C. A. N. Fernando, S. Wickramanayake, S. Punchihewa, L. K. Weerasena, W. D. R. Premasiri, *Phys. Status Solidi A* **1987**, *103*, 491.

[44] Y. Ni, Z. Jin, Y. Fu, *J. Am. Ceram. Soc.* **2007**, *90*, 2966.

[45] X.-D. Gao, X.-M. Li, W.-D. Yu, J.-J. Qiu, X.-Y. Gan, *Thin Solid Films* **2008**, *517*, 554.

[46] B. J. Hathaway, A. A. G. Tomlinson, *Coord. Chem. Rev.* **1970**, *5*, 1.

[47] K. Koyama, M. Tanaka, J. Lee, *Mater. Trans.* **2006**, *47*, 1788.

[48] X. Jiang, Y. Xie, J. Lu, W. He, L. Zhu, Y. Qian, *J. Mater. Chem.* **2000**, *10*, 2193.

[49] L. Tsetseris, *J. Phys. Condens. Matter* **2016**, *28*, 295801.

[50] P. Peumans, S. R. Forrest, *Appl. Phys. Lett.* **2001**, *79*, 126.

[51] D. C. Oertel, M. G. Bawendi, A. C. Arango, V. Bulović, *Appl. Phys. Lett.* **2005**, *87*, 213505.

[52] K. Khojier, H. Savaloni, Z. Sadeghi, *J. Theor. Appl. Phys.* **2014**, *8*, 116.

[53] R. X. Wang, C. D. Beling, S. Fung, a. B. Djurišić, C. C. Ling, S. Li, *J. Appl. Phys.* **2005**, *97*, 033504.

[54] P. Giannozzi, S. Baroni, N. Bonini, M. Calandra, R. Car, C. Cavazzoni, D. Ceresoli, G. L. Chiarotti, M. Cococcioni, I. Dabo, A. Dal Corso, S. de Gironcoli, S. Fabris, G. Fratesi, R. Gebauer, U. Gerstmann, C. Gougoussis, A. Kokalj, M. Lazzeri, L. Martin-Samos, N. Marzari, F. Mauri, R. Mazzarello, S. Paolini, A. Pasquarello, L. Paulatto, C.

Sbraccia, S. Scandolo, G. Sclauzero, A. P. Seitsonen, A. Smogunov, P. Umari, R. M. Wentzcovitch, *J. Phys. Condens. Matter* **2009**, *21*, 395502.

[55] L. Tsetseris, *Phys. Chem. Chem. Phys.* **2016**, *18*, 7837.

[56] L. Tsetseris, *Phys. Chem. Chem. Phys.* **2016**, *18*, 14662.

[57] D. Aldakov, C. Chappaz-Gillot, R. Salazar, V. Delaye, K. Welsby, V. Ivanova, P. Dunstan, *J. Phys. Chem. C* **2014**, *118*, 16095.

[58] N. McIntyre, M. Cook, *Anal. Chem.* **1975**, *47*, 2208.

[59] J. Klein, A. Proctor, D. Hercules, J. Black, *Anal. Chem.* **1983**, *55*, 2055.

[60] C. D. Wagner, J. A. Taylor, *J. Electron Spectros. Relat. Phenomena* **1980**, *20*, 83.

[61] D. Perry, J. Taylor, *J. Mater. Sci. Lett.* **1986**, *5*, 384.

[62] J. Yeh, I. Lindau, *At. Data Nucl. Data Tables* **1985**, *32*, 1.

[63] W. L. Kalb, B. Batlogg, *Phys. Rev. B* **2010**, *81*, 035327.

[64] J. Jeong, J. Seo, S. Nam, H. Han, H. Kim, T. D. Anthopoulos, D. D. C. Bradley, Y. Kim, *Adv. Sci.* **2016**, *3*, 1500269.

[65] B. J. Tremolet de Villers, K. a. O'Hara, D. P. Ostrowski, P. H. Biddle, S. E. Shaheen, M. L. Chabinyc, D. C. Olson, N. Kopidakis, *Chem. Mater.* **2016**, *28*, 876.

[66] S. Chavhan, O. Miguel, H.-J. Grande, V. Gonzalez-Pedro, R. S. Sánchez, E. M. Barea, I. Mora-Seró, R. Tena-Zaera, *J. Mater. Chem. A* **2014**, *2*, 12754.

[67] J. W. Jung, C. Chueh, A. K. Jen, *Adv. Energy Mater.* **2015**, *5*, 1500486.

[68] A. Kojima, K. Teshima, Y. Shirai, T. Miyasaka, *J. Am. Chem. Soc.* **2009**, *131*, 6050.

[69] H.-S. Kim, C.-R. Lee, J.-H. Im, K.-B. Lee, T. Moehl, A. Marchioro, S.-J. Moon, R. Humphry-Baker, J.-H. Yum, J. E. Moser, M. Grätzel, N.-G. Park, *Sci. Rep.* **2012**, *2*, 591.

[70] M. M. Lee, J. Teuscher, T. Miyasaka, T. N. Murakami, Snaith Henry J, *Science* **2012**, *338*, 643.

[71] S. D. Stranks, H. J. Snaith, *Nat. Nanotechnol.* **2015**, *10*, 391.

[72] S. Ye, H. Rao, W. Yan, Y. Li, W. Sun, H. Peng, Z. Liu, Z. Bian, Y. Li, C. Huang, *Adv. Mater.* **2016**, *28*, 9648.

[73] J. Seo, S. Park, Y. C. Kim, N. J. Jeon, J. H. Noh, S. C. Yoon, S. Il Seok, *Energy Environ. Sci.* **2014**, *7*, 2642.

[74] J. H. Park, J. Seo, S. Park, S. S. Shin, Y. C. Kim, N. J. Jeon, H.-W. Shin, T. K. Ahn, J. H. Noh, S. C. Yoon, C. S. Hwang, S. Il Seok, *Adv. Mater.* **2015**, *27*, 4013.

[75] C. Bi, Q. Wang, Y. Shao, Y. Yuan, Z. Xiao, J. Huang, *Nat. Commun.* **2015**, *6*, 7747.

[76] J. Vicente, M. Díaz, *Environ. Sci. Technol.* **2003**, *37*, 1452.

Figures

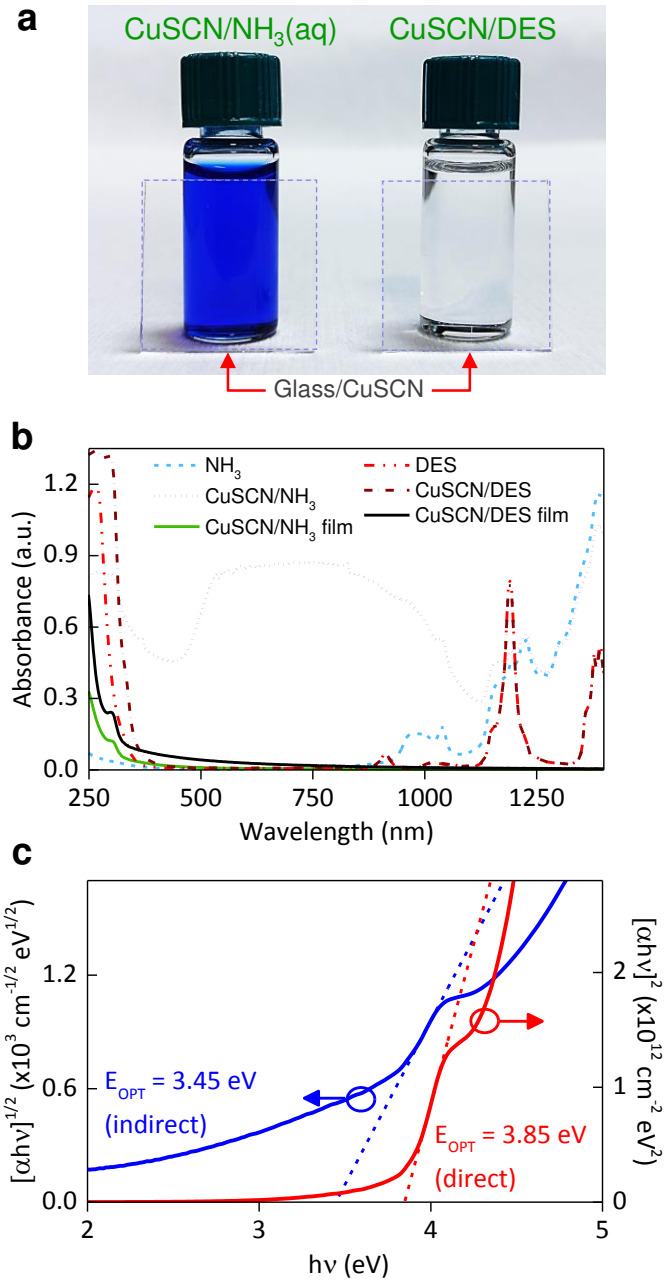

Figure 1. a) Photographs of the vials containing the CuSCN/NH_3(aq) and CuSCN/DES solutions placed behind 2×2 cm^2 glass substrates coated with thin layers of CuSCN. (b) UV-Vis-NIR absorbance spectra of CuSCN solutions, relevant solvents, and thin-films of CuSCN spin-cast on quartz substrates and thermally annealed at 100 ˚C, for comparison. (c) Tauc plots of $(\alpha h\nu)^2$ and $(\alpha h\nu)^{1/2}$ calculated from absorbance spectra of the NH_3(aq)-processed CuSCN layers on quartz. From the linear regions an indirect bandgap of 3.45 (±0.05) eV and a direct bandgap of 3.85 (±0.05) eV, were extracted.

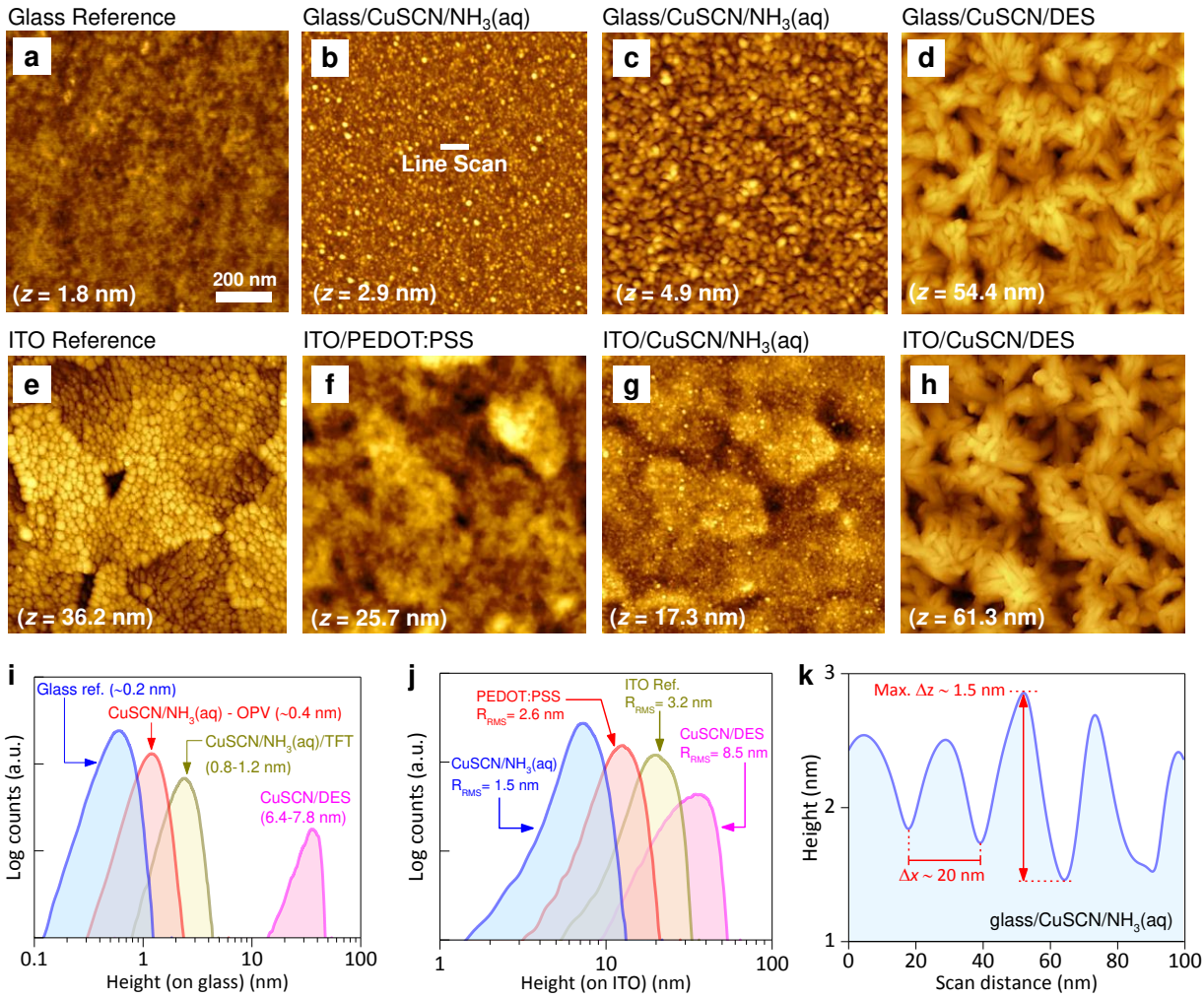

Figure 2. (a-h) AFM surface topography images of various samples, namely; (a) glass substrate, (b) CuSCN/NH_3(aq) spin-cast on glass at 2000 rpm from a 15 mg ml^{-1} solution. (c) CuSCN/NH_3(aq) spin-cast on glass at 800 rpm from a 10 mg ml^{-1} solution. (d) CuSCN/DES spin-cast on glass at 800 rpm from a 10 mg ml^{-1} solution. (e) Glass/ITO surface. (f) PEDOT:PSS spin-cast on glass/ITO at 7000 rpm and annealed at 140 °C. This layer was optimized for HTL applications. (g) CuSCN/NH_3 spin-cast on glass/ITO at 2000 rpm from a 15 mg ml^{-1} solution. (h) CuSCN/DES spin-cast on glass/ITO at 2000 rpm from a 15 mg ml^{-1} solution. (i-j) Height histograms extracted from the AFM data shown in (a-h). The 'OPV' and 'TFT' labels indicate layers spin-cast at 2000 rpm from a 15 mg ml^{-1} solution and at 800 rpm from a 10 mg ml^{-1} solution, respectively. (k) Line scan obtained from the highlighted region in (b). In all topography images, lighter colours correspond to higher regions of the surface where the specified z-values denote the maximum height relative to the minimum at z = 0.

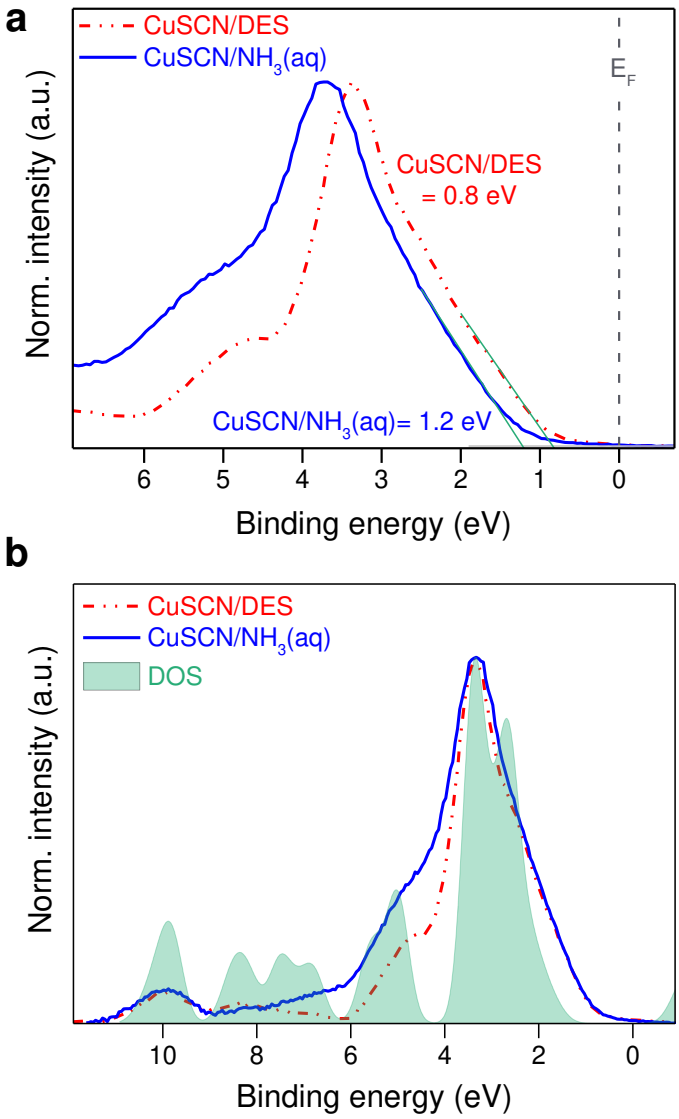

Figure 3. (a) Valence band spectra of CuSCN/DES and CuSCN/NH_3(aq) layers where the position of the VB_{max} with respect to E_F is also shown. (b) Experiment and one electron cross section corrected density of states (DOS) for CuSCN/DES and CuSCN/NH_3(aq) layers from DFT calculations. In (b) the data sets from (a) are aligned to the position of the Cu 3*d* contribution of CuSCN/DES.

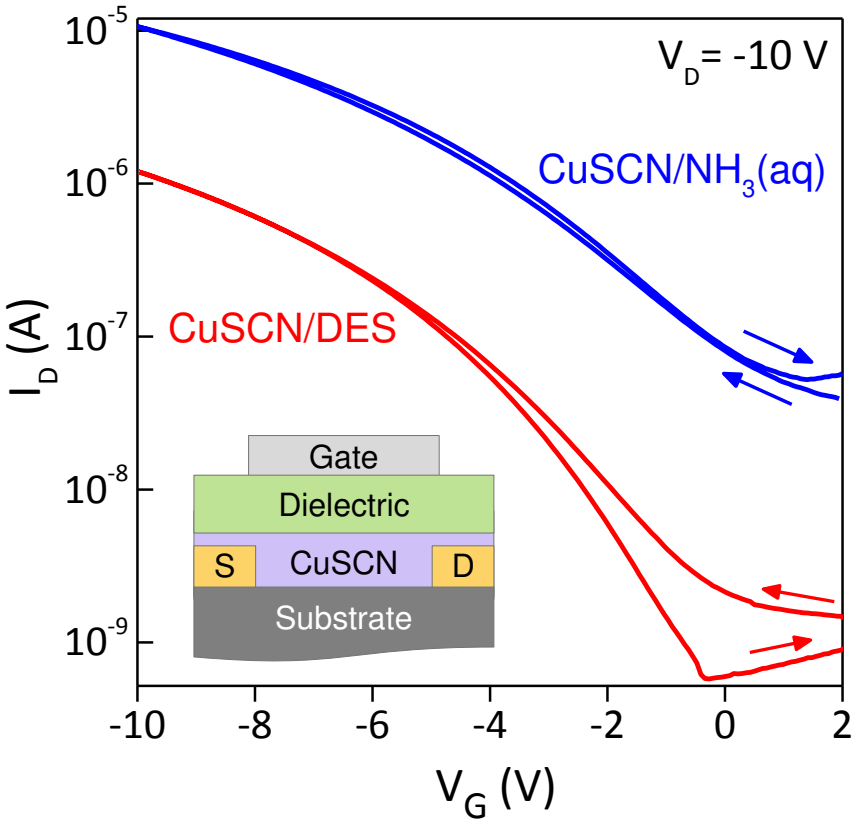

Figure 4. Transfer characteristics of a CuSCN TFT processed via spin-casting from a CuSCN/NH_3(aq) solution. Inset shows a schematic of the staggered TG-BC transistor architecture employed with Au S-D contacts and Al gate electrode. The channel dimensions of the transistor are L = 30 µm and W = 1000 µm.

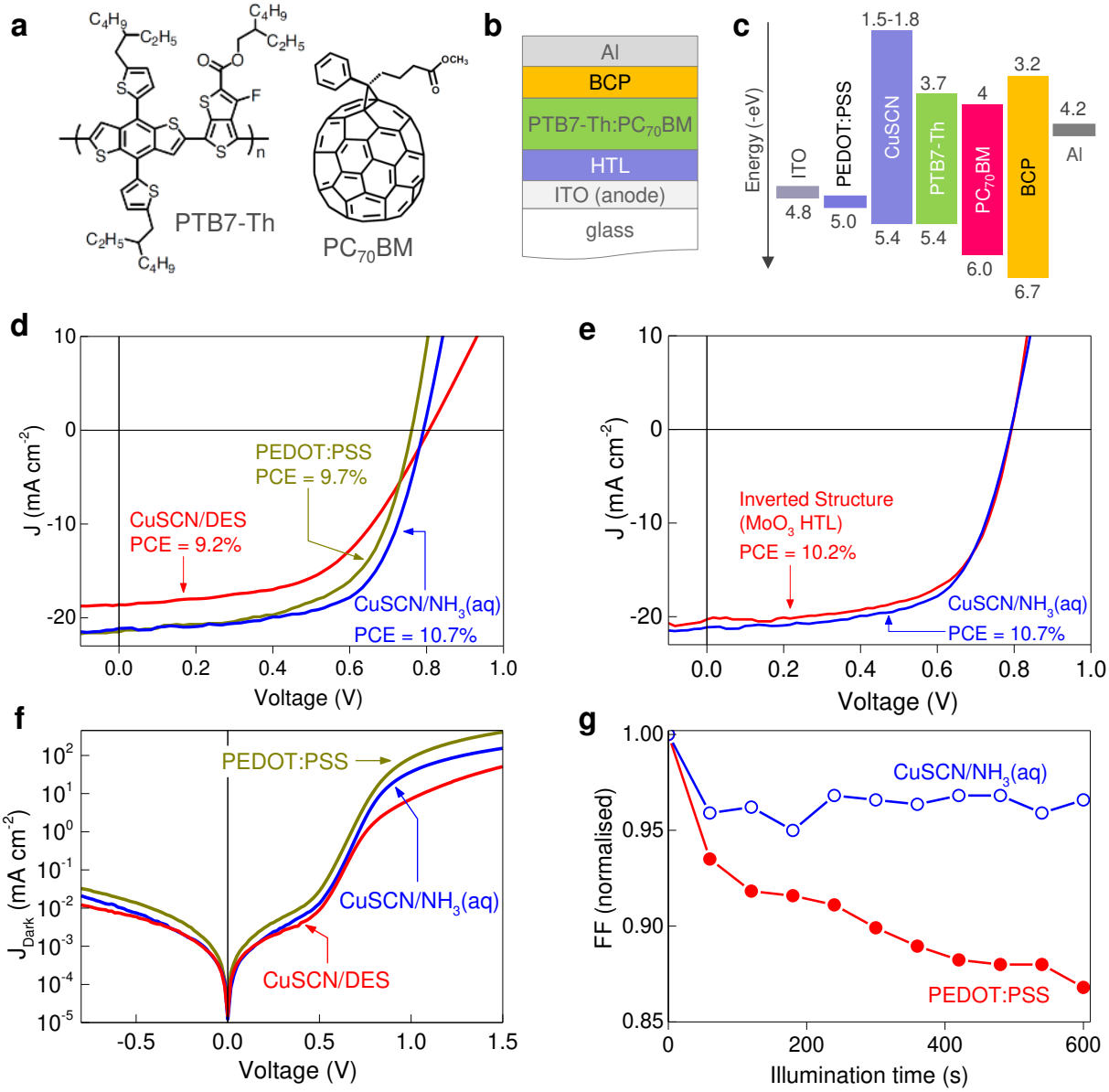

Figure 5. (a) Chemical structures of the active blend components PTB7-Th and $PC_{70}BM$. (b) Schematic cross-section of the standard cell architecture employed. (c) Energetics of the various materials employed. (d) J–V characteristics measured under simulated solar light illumination for standard PTB7-Th:$PC_{70}BM$ OPV cells based on three different HTLs, namely; CuSCN/DES, CuSCN/NH_3(aq) and PEDOT:PSS. (e) J-V characteristics of a standard and an inverted PTB7-Th:$PC_{70}BM$ cell. In the case of the inverted cell, MoO_3 was used as the HTL. (f) Dark J-V characteristics measured for the three OPV cells shown in (d). (g) Normalized stability curves of FF of samples with PEDOT:PSS and CuSCN/NH_3(aq) HTLs.

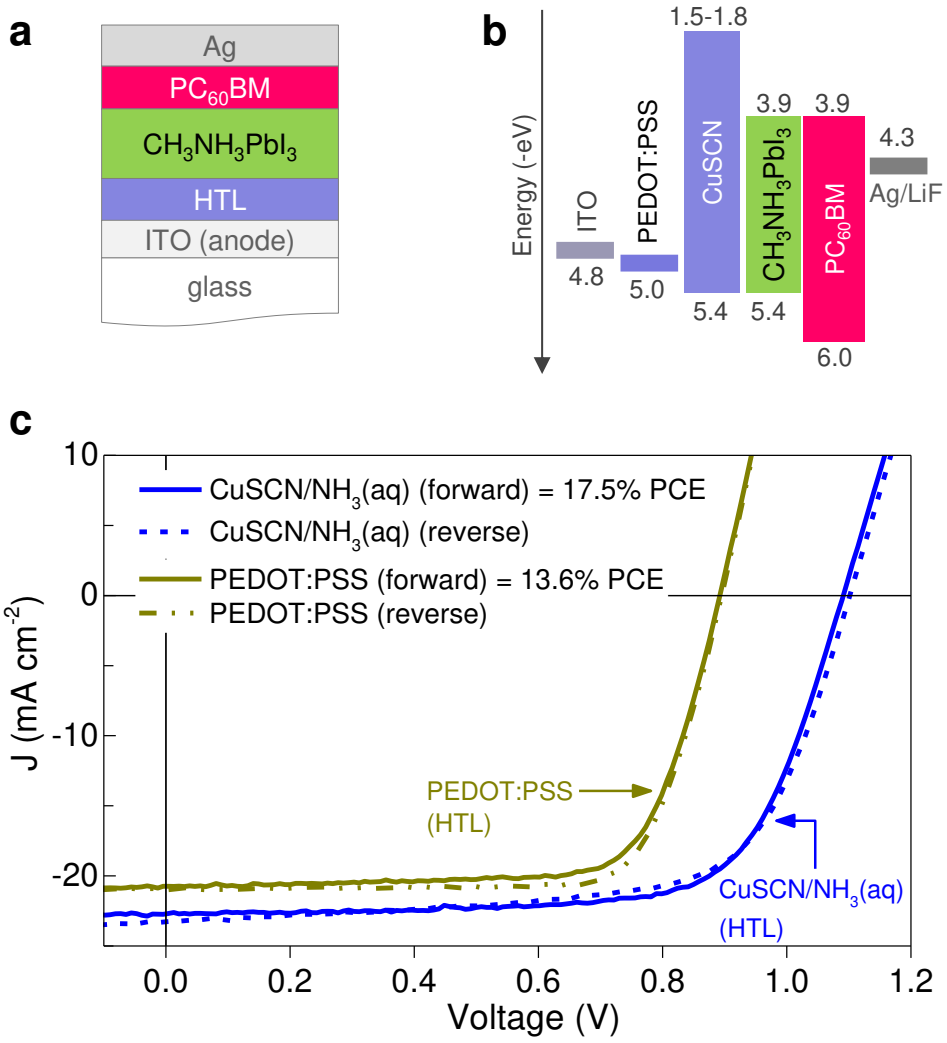

Figure 6. (a) Schematic cross-section of the cell architecture employed, and (b) corresponding material energetics. (c) J-V characteristics measured under simulated solar illumination for two $CH_3NH_3PbI_3$ solar cells based on CuSCN/NH_3(aq) and PEDOT:PSS HTLs.

Table 1. Summary of the device parameters of TG-BC CuSCN transistors processed from NH_3(aq) and DES solutions. The channel length and width of all transistors were 30 and 1000 µm, respectively.

Solvent	μ_{lin}[a] ($cm^2V^{-1}s^{-1}$)	μ_{sat}[a] ($cm^2V^{-1}s^{-1}$)	On/off ratio	V_{on}[b] (V)	V_{th}[b] (V)	SS (V dec^{-1})
DES	0.01 (0.01)	0.01 (0.02)	2 x10^3	-0.3	-3.1	1–2
NH_3(aq)	0.04 (0.05)	0.05 (0.07)	4 x10^2	1.0	-2.1	2–3

[a] Mean values obtained from five TFTs; data from the 'champion' device is given in brackets. The standard deviation is 0.01 $cm^2V^{-1}s^{-1}$.
[b] Mean values extracted from saturation regime data. The standard deviation is 0.3 V.

Table 2. Summary of operating parameters for PTB7-Th:$PC_{70}BM$ OPV cells made with different HTLs.

HTL[a]	J_{SC} (mA cm^{-2})	V_{OC} (V)	FF	PCE (%)
PEDOT:PSS	19.2 (21.5)	0.76 (0.77)	0.60 (0.60)	9.10 (9.67)
1 × CuSCN/NH_3(aq)[b]	20.1 (20.5)	0.78 (0.78)	0.62 (0.63)	9.30 (10.12)
2 × CuSCN/NH_3(aq)[b]	20.0 (21.1)	0.79 (0.80)	0.63 (0.63)	10.01 (10.70)
3 × CuSCN/NH_3(aq)[b]	18.0 (20.1)	0.78 (0.78)	0.59 (0.61)	9.25 (9.46)
CuSCN/DES	19.4 (20.8)	0.79 (0.80)	0.54 (0.57)	8.33 (9.15)
MoO_3 (Inverted)	19.0 (20.3)	0.79 (0.80)	0.64 (0.65)	9.68 (10.20)

[a] Mean values obtained from eight cells; data from the 'champion' cell is given in brackets.
[b] Data from cells containing single, double and triple-spun CuSCN/NH_3(aq) layers.

Table 3. Summary of operating parameters for $CH_3NH_3PbI_3$ perovskite solar cells containing CuSCN/NH_3(aq) and PEDOT:PSS HTLs.

HTL[a]	J_{SC} (mA cm^{-2})	V_{OC} (V)	FF	PCE (%)
PEDOT:PSS	18.3 (20.7)	0.89 (0.90)	0.73 (0.73)	12.4 (13.6)
CuSCN/NH_3(aq)	22.3 (22.7)	1.09 (1.10)	0.71 (0.71)	17.2 (17.5)

[a] Mean values obtained from four cells; data from the 'champion' cell is given in brackets.

Dissolution of copper thiocyanate (CuSCN) in aqueous ammonia enables processing of superior quality hole transporting layers at low temperature in ambient air. Transistors and solar cells based on these CuSCN layers exhibit mobilities close to 0.1 cm^2/Vs and power conversion efficiency of 10.7% and 17% for organic bulk-heterojunction and organometal halide cells, respectively.

Keywords: Copper(I) thiocyanate; hole transport layers; organic solar cells; perovskite solar cells; transparent semiconductors and transistors

Nilushi Wijeyasinghe, Anna Regoutz, Flurin Eisner, Tian Du, Leonidas Tsetseris, Yen-Hung Lin, Hendrik Faber, Pichaya Pattanasattayavong, Jinhua Li, Feng Yan, Martyn A. McLachlan, David J. Payne, Martin Heeney and Thomas D. Anthopoulos

Copper(I) Thiocyanate (CuSCN) Hole-Transport Layers Processed from Aqueous Precursor Solutions and Their Application in Thin-Film Transistors and Highly Efficient Organic and Organometal Halide Perovskite Solar Cells

ToC Figure

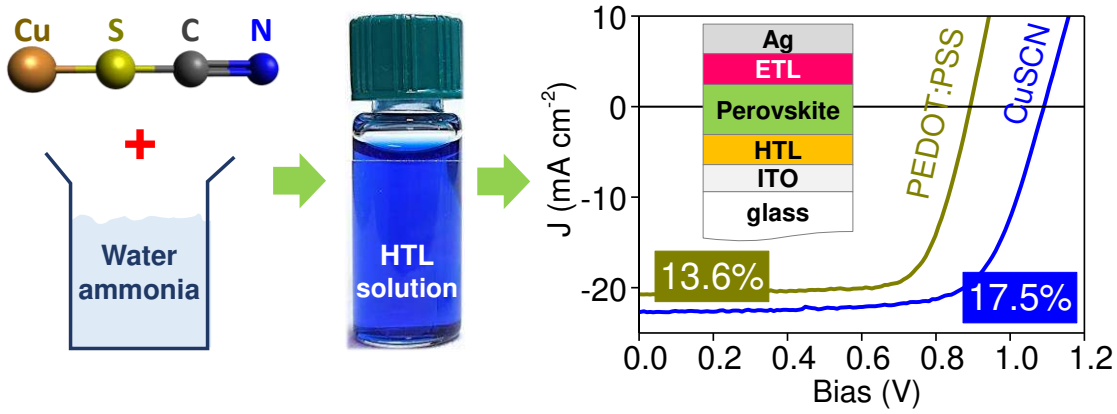

****

Supporting Information

Copper(I) Thiocyanate (CuSCN) Hole-Transport Layers Processed from Aqueous Precursor Solutions and Their Application in Thin-Film Transistors and Highly Efficient Organic and Organometal Halide Perovskite Solar Cells

*Nilushi Wijeyasinghe, Anna Regoutz, Flurin Eisner, Tian Du, Leonidas Tsetseris, Yen-Hung Lin, Hendrik Faber, Pichaya Pattanasattayavong, Jinhua Li, Feng Yan, Martyn A. McLachlan, David J. Payne, Martin Heeney and Thomas D. Anthopoulos**

S1. UV-Vis-NIR Spectroscopy

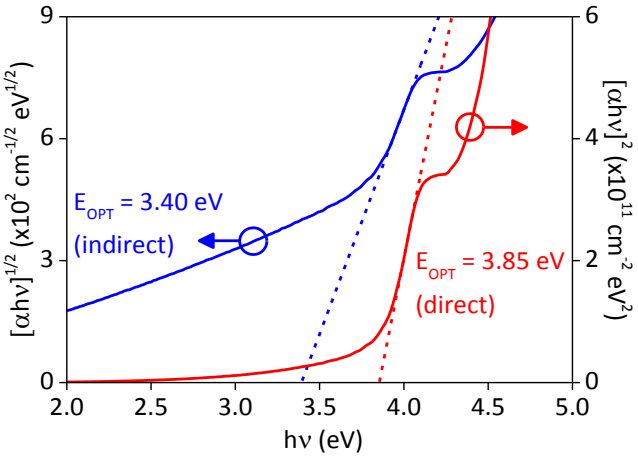

Figure S1. Plots of $(\alpha h\nu)^2$ and $(\alpha h\nu)^{1/2}$ calculated from absorbance measurements of a DES-processed CuSCN layer on quartz. The linear regions correspond to an indirect bandgap of 3.40 (±0.05) eV and a direct bandgap of 3.85 (±0.05) eV.

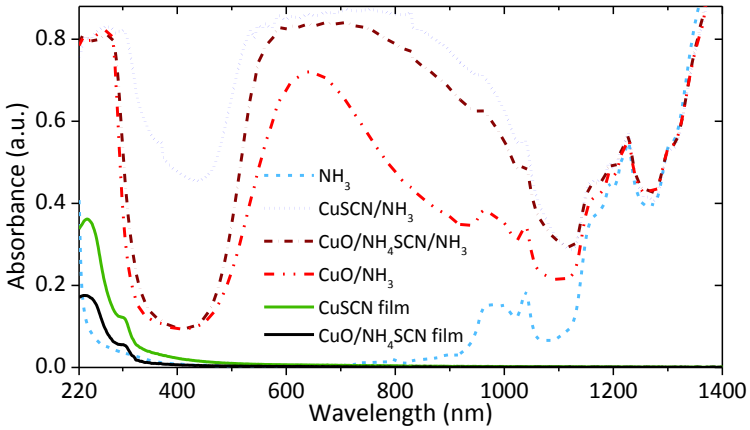

Figure S2. UV-Vis-NIR absorbance spectra of the aqueous ammonia-based solutions containing CuSCN and CuO/NH_4SCN precursors; the spectra of layers spin-cast on quartz and annealed at 100 ˚C are shown for comparison. The deep blue colour of $CuSCN/NH_3$ and $CuO/NH_4SCN/NH_3$ solutions correspond to strong absorption in the 550–700 nm spectral region. Notably, the $CuO/NH_4SCN/NH_3$ and $CuSCN/NH_3$ spectra exhibit remarkably similar

absorption features, but in contrast, CuO/NH_3 exhibits a considerable difference in absorbance at the 550–1150 nm region due to the absence of thiocyanate ions. Furthermore, the intensity of the broad transmittance peak at ~400 nm differs significantly between solutions with CuSCN and CuO precursors. This is attributed to the lower solubility of CuO in aqueous NH_3. The latter forms a saturated solution at 10 mg ml^{-1} that contains a smaller concentration of copper ions relative to the CuSCN/NH_3 solution.

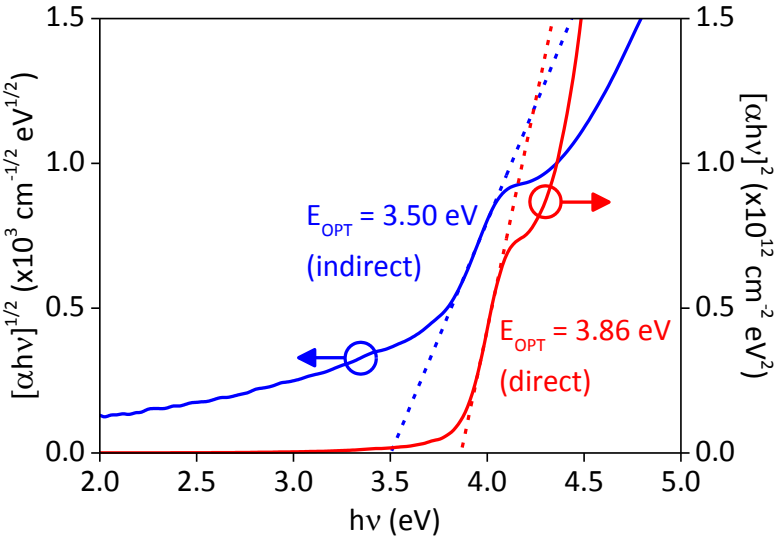

Figure S3. Plots of $(\alpha h\nu)^2$ and $(\alpha h\nu)^{1/2}$ calculated from absorbance measurements of an ammonia-processed CuSCN layer spin-cast on quartz from a CuO/NH_4SCN precursor formulation. From the linear regions of the plots an indirect bandgap of 3.50 (±0.05) eV and a direct bandgap of 3.86 (±0.05) eV, were extracted.

S2. Atomic Force Microscopy (AFM)

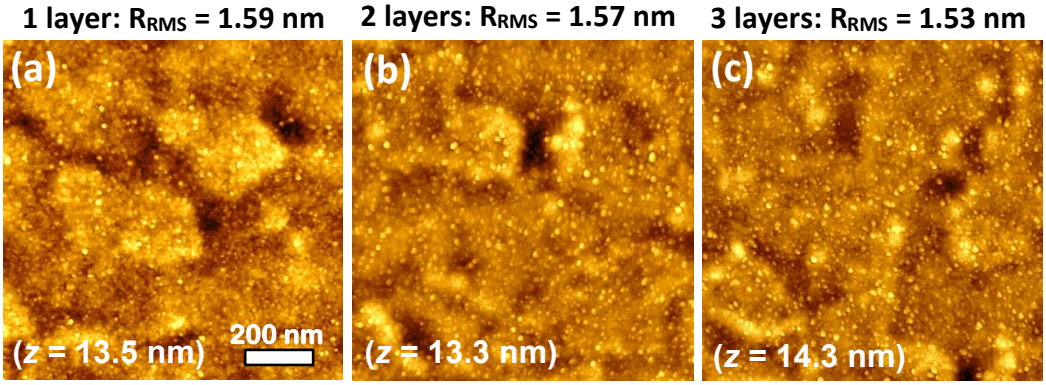

Figure S4. Topography AFM images (scan area of 1 μm^2) of ammonia-processed CuSCN HTLs deposited on glass/ITO. (a) The CuSCN layer was spin-cast at 2000 rpm from a 15 mg ml^{-1} CuSCN precursor solution and annealed at 100 °C. (b) and (c) show the topography images of CuSCN layers formed after 2 and 3, respectively, sequential spin-casting rounds of CuSCN using the same growth conditions. In all images, lighter colours correspond to higher regions

of the surface and the specified z-values denote the maximum height relative to the minimum at z = 0.

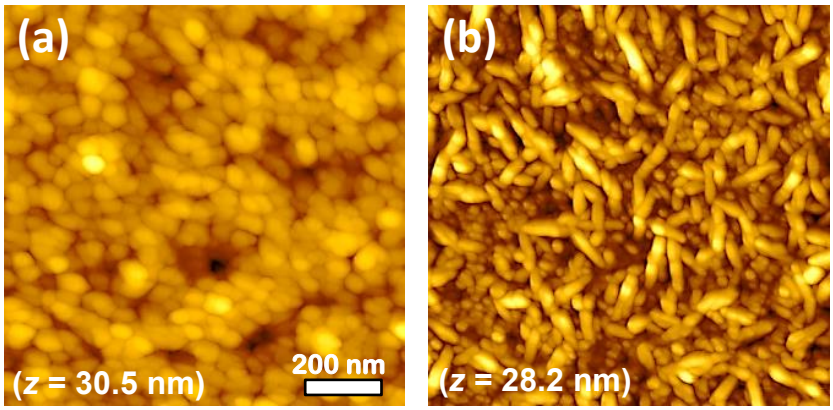

Figure S5. Topography AFM images (scan area of 1 μm^2) of CuSCN/DES layers spin-cast on glass at 800 rpm from 10 mg ml^{-1} solutions and annealed at 100 °C in air. (a) A CuSCN layer that is dominated by the presence of spherical grains and exhibits surface R_{RMS} = 3.2 nm. (b) A CuSCN layer that is dominated by elongated grains, where R_{RMS}=3.9 nm. Lighter colours correspond to higher regions of the surface and the specified z-values denote the maximum height relative to the minimum at z = 0.

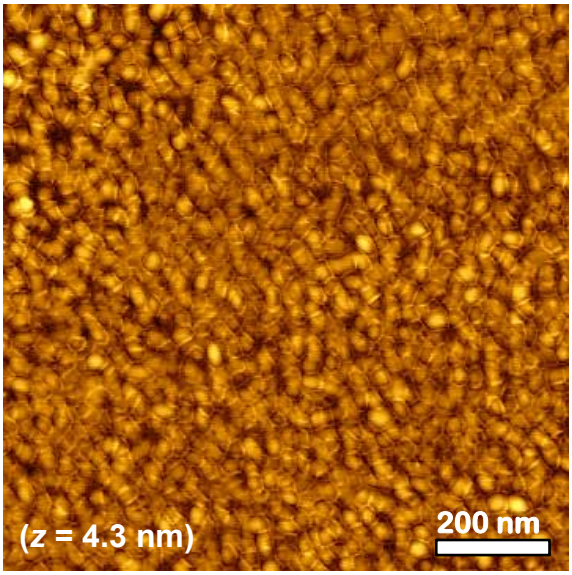

Figure S6. Topography AFM image (scan area of 1 μm^2) of a CuSCN layer spin-cast on glass at 800 rpm from a solution that consisted of CuO and NH_4SCN dissolved in aqueous ammonia. The nanocrystalline film (R_{RMS} = 0.6 nm) exhibits a similar morphology to the CuSCN layers processed from CuSCN/NH_3(aq). Lighter colours correspond to higher regions of the surface topography with the maximum height feature z being 4.3 nm.

S3. X-ray Photoelectron Spectroscopy

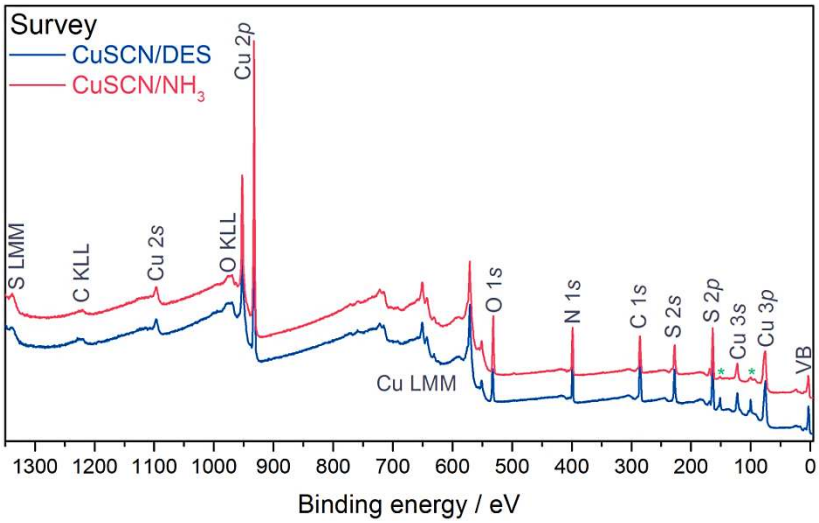

Figure S7. Survey spectra of CuSCN/DES and CuSCN/NH_3 indicating core levels and Auger lines. The lines at 100 and 150 eV, marked with an asterisk, correspond to the Si 2*p* and 2*s* core lines of the substrate.

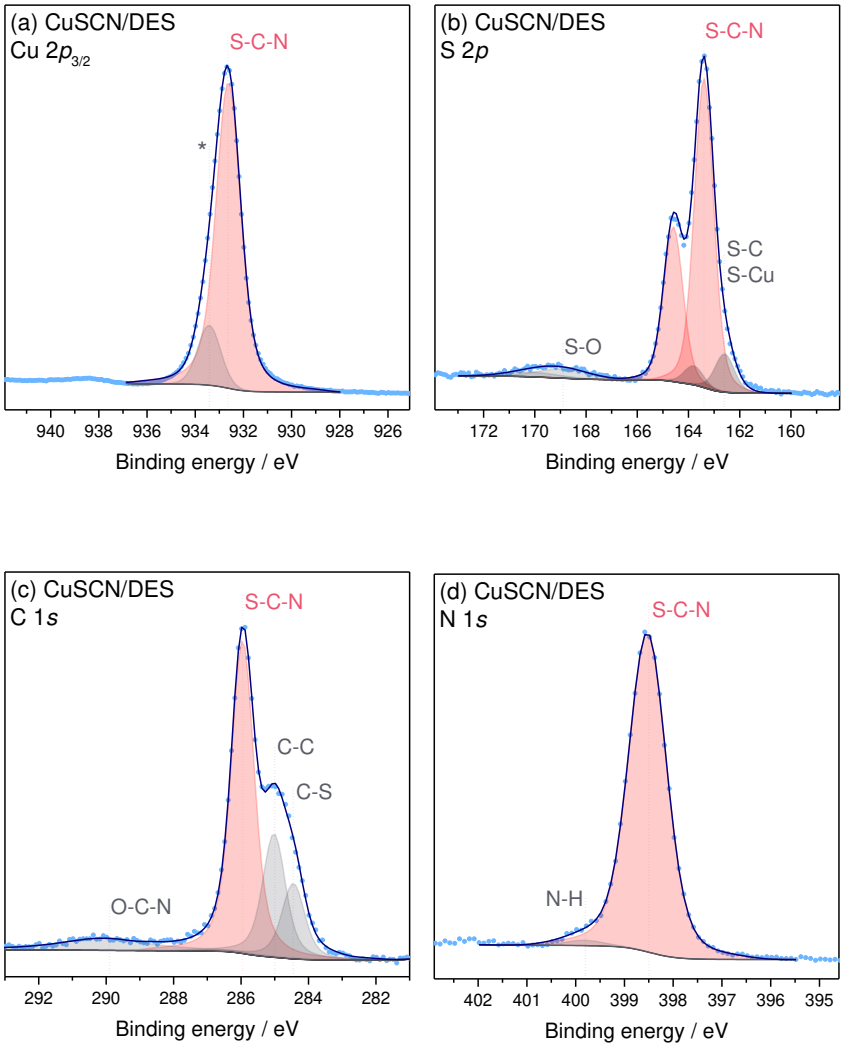

Figure S8. Peak fit analysis of the core level spectra measured for CuSCN layers processed from CuSCN/DES including: (a) Cu $2p_{3/2}$, (b) S $2p$, (c) C $1s$, and (d) N $1s$.

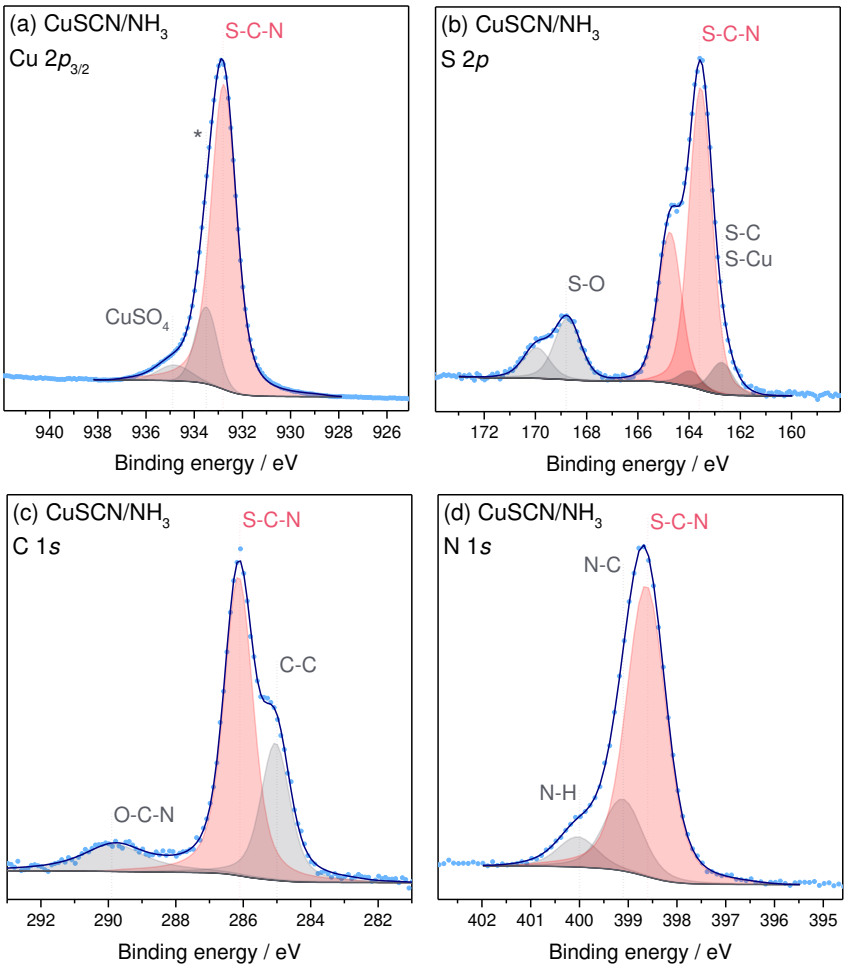

Figure S9. Peak fit analysis of the core level spectra measured for CuSCN layers processed from CuSCN/NH_3(aq) including: (a) Cu $2p_{3/2}$, (b) S $2p$, (c) C $1s$, and (d) N $1s$.

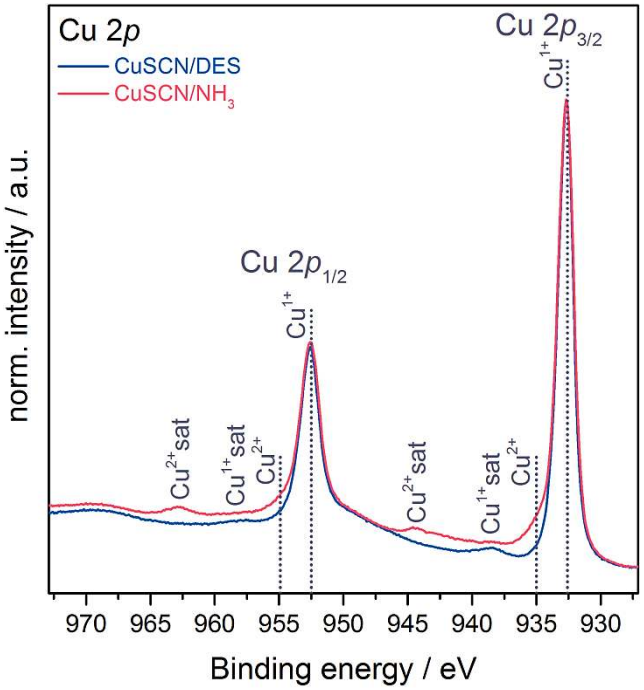

Figure S10. Cu 2*p* core level spectra of CuSCN layers processed from CuSCN/DES and CuSCN/NH_3(aq) solutions including satellite structures.

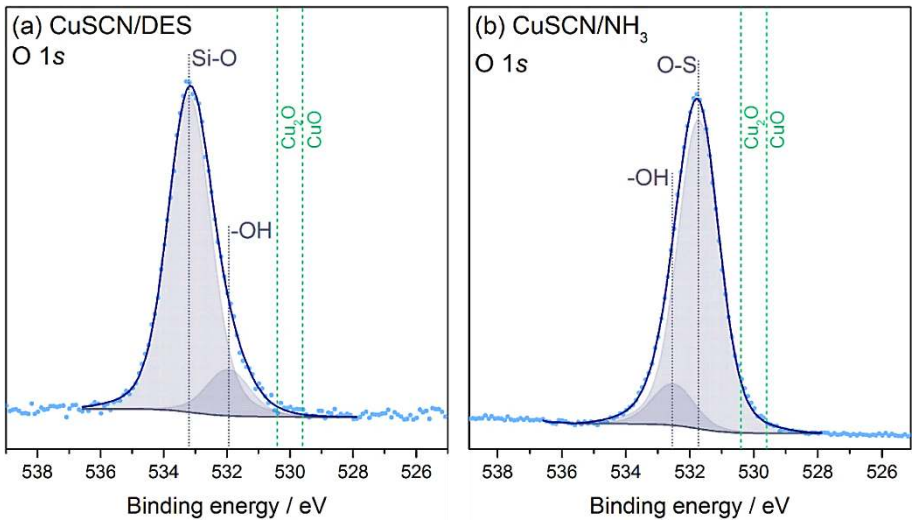

Figure S11. Peak fit analysis of the O 1*s* core level spectra of; (a) CuSCN/DES and (b) CuSCN/NH_3(aq).

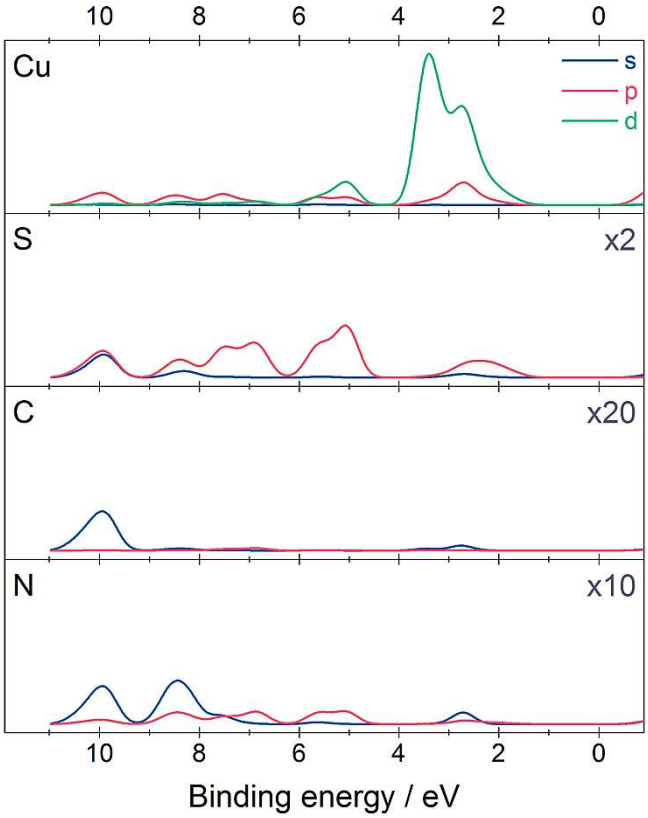

Figure S12. One electron cross section weighted partial densities of states (PDOS) for CuSCN from DFT calculations.

Table S1. Binding energy positions of core levels for both CuSCN samples from peak fit analysis of XPS data. Peaks marked with an asterisk correspond to the contribution from CuSCN itself.

Sample	Cu $2p_{3/2}$	S $2p_{3/2}$	C 1*s*	N 1*s*
CuSCN/DES	932.6*	162.6 163.4* 168.9	284.5 285.0 286.0* 290.1	398.5* 399.8
CuSCN/NH_3(aq)	932.8* 934.9	162.7 163.6* 168.8	285.0 286.1* 289.9	398.6* 399.1 400.0

Table S2. Elemental ratios from peak fit analysis in atomic % (at%).

Sample	at% Cu	at% S	at% C 1*s*	at% N 1*s*
CuSCN/DES	27.1	24.7	23.6	24.7
CuSCN/NH_3(aq)	33.6	22.5	21.5	22.3

S4. Electrical Characterization of Thin-Film Transistors

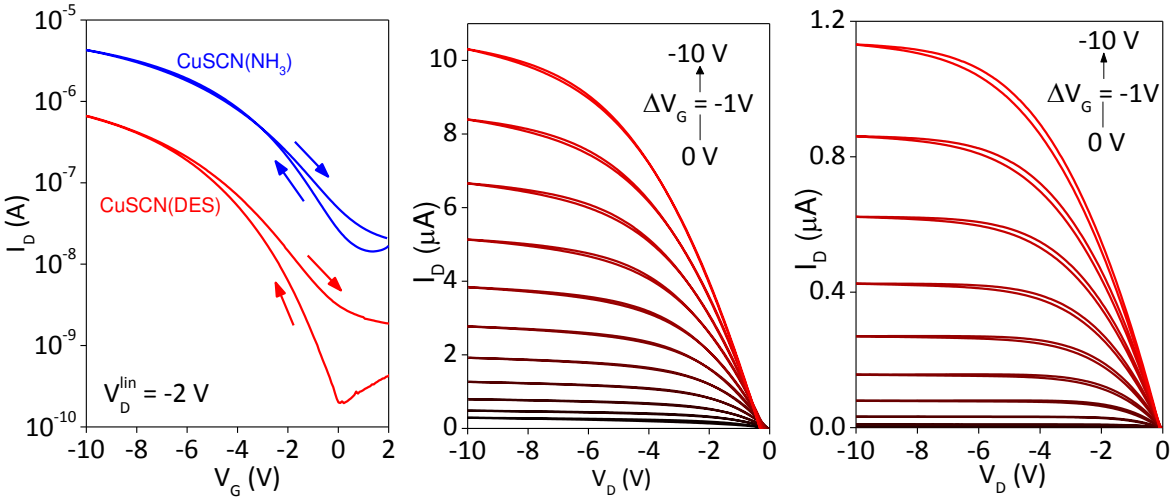

Figure S13. Electrical characteristics of TG-BC CuSCN TFTs based on P(VDF-TrFE-CFE) polymer as the gate dielectric. The TFT channel dimensions employed are L = 30 µm and W = 1000 µm. (left) Transfer characteristics measured in the linear regime. Output characteristics of CuSCN TFTs processed from NH_3(aq) (middle), and DES (right).

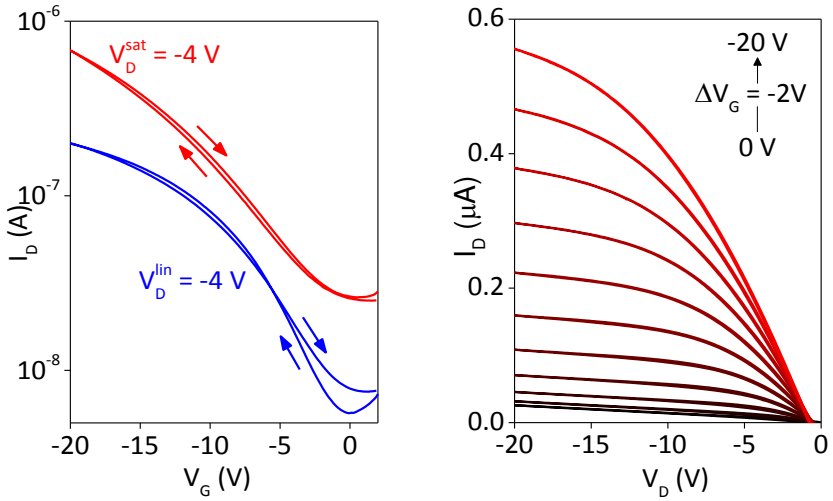

Figure S14. Electrical characterization of a TG-BC CuSCN-based TFT with a P(VDF-TrFE-CFE) polymer dielectric, which has channel dimensions of L = 30 µm and W = 1000 µm. Transfer (Left) and output (right) characteristics of a CuSCN TFT processed from an aqueous CuO/NH_4SCN precursor solution.

S5. Characterization and Stability Tests of Perovskite Solar Cells

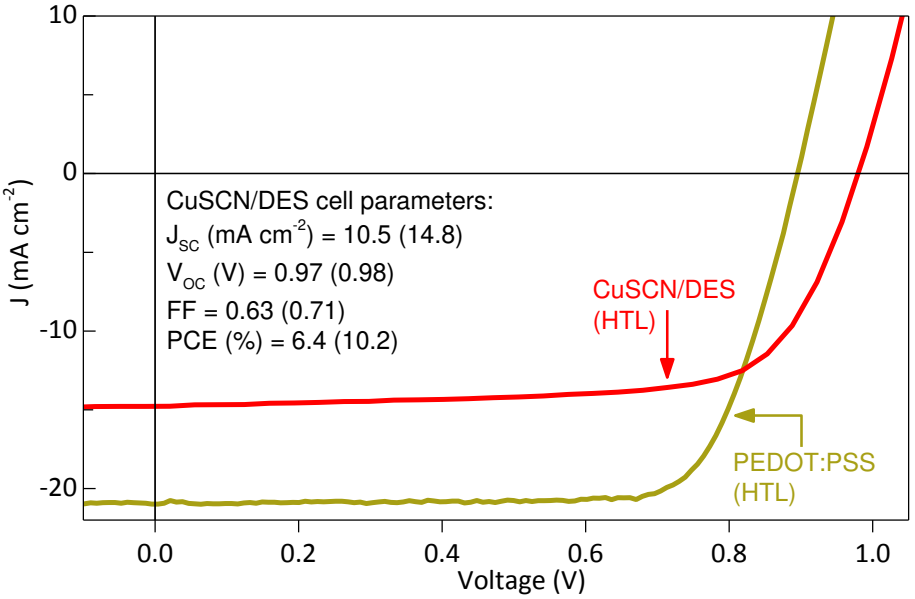

Figure S15. J-V characteristics measured under simulated 1-sun solar illumination for a $CH_3NH_3PbI_3$ solar cell based on a CuSCN/DES HTL; the characteristics of an identical cell containing a PEDOT:PSS HTL is shown for comparison. Due to the low yield of devices exhibiting correct solar cell function, only a single CuSCN/DES-based device was characterised. The key parameters specified indicate the first dataset recorded, with the best of three datasets given in brackets. Solar cells with CuSCN/DES HTLs show inferior performance and lower stability relative to those with PEDOT:PSS HTLs; the physical mechanisms behind the low device stability are yet to be determined and are beyond the scope of this work.

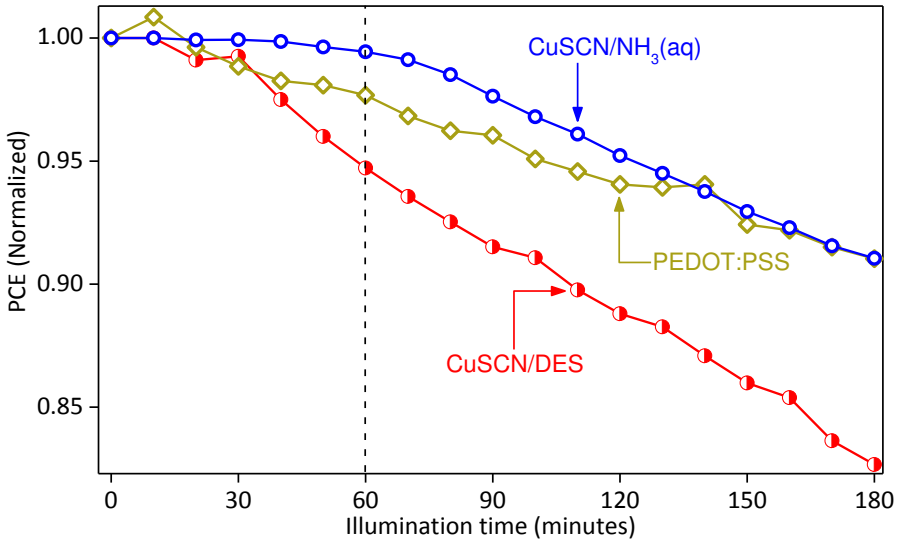

Figure S16. Normalized stability curves of PCE of $CH_3NH_3PbI_3$ solar cells based on different HTLs. The data was recorded in a nitrogen atmosphere during a constant AM1.5 simulated solar illumination period of 3 h. Compared to solar cells utilizing CuSCN/DES and PEDOT:PSS HTLs, devices containing CuSCN/NH_3(aq) HTLs exhibit excellent operating stability during the first 1 hr illumination period, and superior stability over the 3 h test period. Note that the data are normalised relative to the PCE value at time = 0 min.